An analytical method to quantify the statistics of energy landscapes in random solid solutions

Ritesh Jagatramka Chu Wang Matthew Daly*

Department of Civil, Materials, and Environmental Engineering, University of Illinois Chicago – 842 W. Taylor St., 2095 ERF (MC 246), Chicago, IL, 60607, United States

ABSTRACT

Recent studies of concentrated solid solutions have highlighted the role of varied solute interactions in the determination of a wide variety of mesoscale properties. These solute interactions emerge as spatial fluctuations in potential energy, which arise from local variations in the chemical environment. Although observations of potential energy fluctuations are well documented in the literature, there remains a paucity of methods to determine their statistics. Here, we present a set of analytical equations to quantify the statistics of potential energy landscapes in randomly arranged solid solutions. Our approach is based on a reparameterization of the relations of the embedded-atom method in terms of the solute coordination environment. The final equations are general and can be applied to different crystal lattices and energy landscapes, provided the systems of interest can be described by sets of coordination relations. We leverage these statistical relations to study the cohesive energy and generalized planar fault energy landscapes of several different solid solutions. Analytical predictions are validated using molecular statics simulations, which find excellent agreement in most cases. The outcomes of this analysis provide new insights into phase stability and the interpretation of 'local' planar fault energies in solid solutions, which are topics of ongoing discussion within

^{*}Corresponding author: <u>mattdaly@uic.edu</u> (M. Daly)

the community.

Keywords: Solid solutions; High Entropy Alloys; Embedded-Atom Method; Cohesive Energy; Planar Fault Energy

1. INTRODUCTION

Recent interest in concentrated systems has spurred research activity in the metallurgy of multicomponent solid solutions. These efforts have produced new physical insights into the role of solute interactions, with a focus on behaviors that emerge in concentrated mixtures. Studies in high entropy alloys (HEA)s, which are considered here as a subset of concentrated solid solutions, are perhaps the most visible. Notable examples include investigations of soluteinduced lattice distortion [1-5], variations in dislocation glide barriers [6-13], and solute effects on planar and twinning fault energies [14-18]. While the effects of solute can be revealed by computational studies and inferred by experiments (e.g., as in Refs. [19-21]), new theoretical challenges have arisen concerning the prediction of material properties. For instance, traditional solute theories such as those for solid solution strengthening [22–25], find limited applicability in concentrated systems [8,13]. In many cases, the shortcomings of traditional theories can be traced to the irregular nanoscale fluctuations in the potential energy (PE) landscape, as demonstrated in recent theoretical advancements from Curtin and coworkers [6,8,13]. These topology-induced PE fluctuations emerge from local variations in composition and solute interactions, whose effect becomes significant in concentrated solid solutions. Perhaps the most basic example of such a PE landscape is that of cohesive energy, but more complicated landscapes such as that of the Peierls barrier and the generalized planar fault energy (GPFE) are familiar to the community.

New literature continues to emerge that highlights the challenges and opportunities these fluctuating PE landscapes offer to the physical metallurgy of concentrated solid solutions [9,26,27]. Some notable progress has been made in recent works in treating variable PE landscape problems. For instance, Varvenne et al. [28] have developed an effective medium model, based on the embedded-atom method (EAM) [29–31], which homogenizes the effects of solute in randomly arranged solid solutions. Several studies have leveraged this model to calculate material properties in concentrated systems including lattice parameters [16,32–35], elastic constants [16,32–35], cohesive energies [16,32], and stacking fault energies [16,34,35]. While this method is suitable for the calculation of homogenized bulk properties, a limitation arises when predicting material phenomena at length scales that approach those of the nanoscale fluctuations in the PE landscape. Certainly, there is a building body of literature focused on the study of material properties that are controlled by the fluctuations in the PE landscape of concentrated solid solutions. For example, Curtin and coworkers [6,8,13] have developed a method to measure the fluctuations in dislocation glide barriers that emerge from varied dislocation-solute and solute-solute interactions in solid solutions. Additionally, Zhang et al. [9] have incorporated a stochastic coefficient function into the classic Peierls-Nabarro model to predict a distribution of Peierls stresses in HEAs. Ghazisaeidi and coworkers [36,37] report the statistics of a 'local' stacking fault energy that arises due to the varied solute interactions in the vicinity of planar defects. The qualitative link between these local stacking fault energies and the varied local chemical environment in concentrated solid solutions has been studied by Zhao et al. [17] and Ma and coworkers [38,39]. Undoubtedly, this new body of literature highlights the emergence of a variable 'local' property that arises from the statistical distribution of solute interactions that are inherent to concentrated solid solutions.

Although the observational connection between fluctuations in the PE landscape and the emergence of local material properties is now well established, there is a paucity of methods to directly calculate these fluctuations from system topology inputs. Specifically, analytical techniques that link the statistical variations in composition and neighbor pairings in solid solutions with fluctuations in PE landscapes remain sparse. To the authors' knowledge, the only example of a direct analytical relation is found in a recent study by Curtin and coworkers [6], where the specific use-case of fluctuations in solute-solute interactions during dislocation slip is studied. This dearth of analytical approaches limits the broad exploration of new theoretical models, where inputs for compositional and structural PE landscape fluctuations must be measured from atomistics [8] or take on assumed forms [9].

Here, we present an analytical approach to quantify the statistics of fluctuations in PE landscapes of randomly arranged solid solutions. This framework is developed here for EAM-type relations, which are commonly used to model the metallic bonding of alloys. These relations are applicable to randomly arranged solid solutions in any crystal system with arbitrary numbers of components and concentrations. To demonstrate this approach, we consider two PE landscapes: those of the cohesive energy and the GPFE. These landscapes are selected due to their roles in phase stability and in defining the intrinsic competition between deformation mechanisms. For the purposes of analyzing phase stability, examination of cohesive energy landscapes is performed on both face-centered cubic (FCC) and hexagonal

close-packed (HCP) solid solutions. Application of this method to other PE landscapes is possible, with some limitations discussed later. The outcomes of this work provide analytical tools to study the statistics of PE fluctuations, which are important to the advancement of several classes of theories in the physical metallurgy of solid solutions.

2. ANALYTICAL DERIVATION OF STATISTICAL QUANTITIES

The primary challenge in quantifying the fluctuations in the PE landscape lies in the variations in composition and arrangement of neighbors that are encountered when sampling small volumes in solid solution ensembles. Indeed, sampling of n_c solute atoms in a randomly arranged solid solution produces a Gaussian distribution of mean compositions of the form $G^X \sim \left(\bar{C}^X, \sqrt{\frac{\bar{C}^X(1-\bar{C}^X)}{n_C}}\right)$, where \bar{C}^X is the system-level composition of element X presented as a molar fraction. In this notation, the first parameter is the distribution average, and the second parameter is the standard deviation. Furthermore, capitalized statistical parameters refer to population properties and lowercase symbols refer to samples drawn from these populations. By a similar calculation, the solute pairings from n_s samples of two randomly selected solutes form a distribution with parameters $G^{XY} \sim \left(\bar{C}^X \bar{C}^Y, \sqrt{\frac{\bar{C}^X \bar{C}^Y (1 - \bar{C}^X \bar{C}^Y)}{n_S}}\right)$. Here, the term solute pairing refers to the combinations of chemical pairs XY that exist in a multicomponent system. For instance, in a binary system with two atom types, these combinations would be 11, 12, 21, and 22. Figure 1 presents the solute pairing statistics for a numerical simulation of a theoretical ternary system with randomly drawn samples, which mimics the organization of solute in a randomly arranged solid solution. As shown in the figure, the fluctuations in composition and solute pairings around the system averages are significant, which underscores the varied chemical environment encountered in solid solutions. A derivation of the statistical parameters (i.e., the standard deviation) of these distributions is provided in Appendix A.

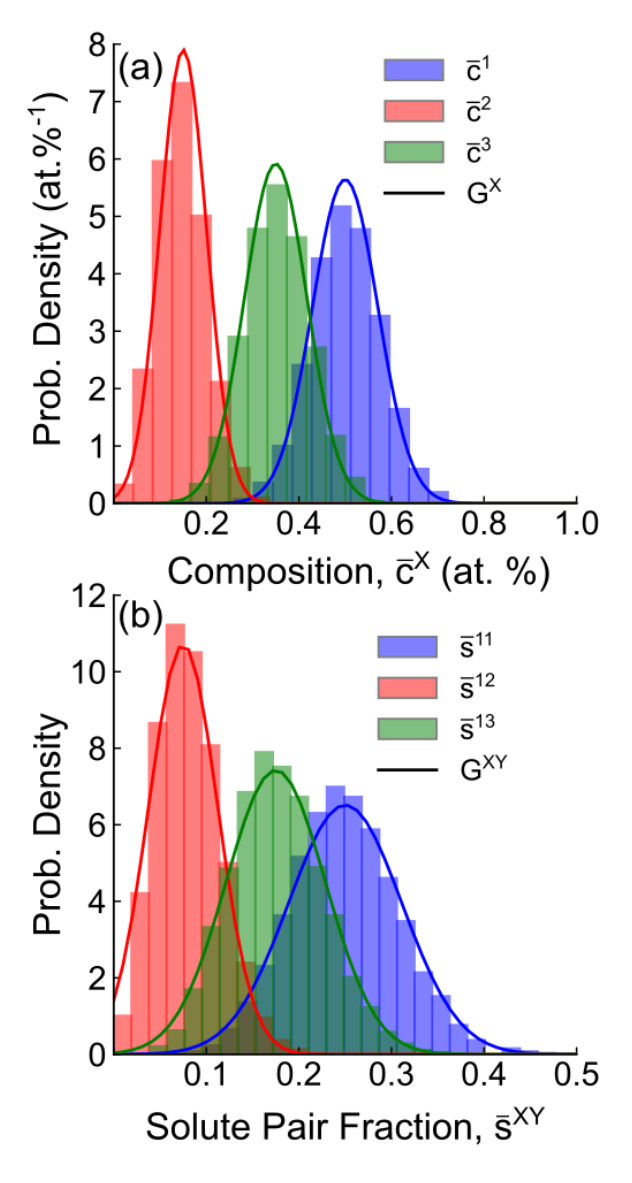


Figure 1: (a) A numerical simulation of sampled compositions for a randomly arranged solid solution. The sample means (\bar{c}^X) are plotted as a histogram and the statistical distribution (G^X) is plotted in solid stroke. Samples $(n_c = 50)$ were randomly collected from a ternary system of 10^6 atoms with an overall composition of $\bar{C} = (0.5, 0.15, 0.35)$. (b) The distribution of sampled solute pair fractions $(n_s = 50)$ in the same system. The sample means (\bar{s}^{XY}) are presented as a fraction and are plotted with the statistical distribution (G^{XY}) for 3 of 9 possible solute pairings, where \bar{s}^{XY} and \bar{s}^{YX} are separately expressed. The distributions in (a) and (b) have been sampled more than 2×10^4 times with replacement.

Within the context of energy landscapes, the composite effect of the statistical variations in local composition and solute pairings give rise to the fluctuations observed in the PE. An

example of this effect on the per atom site energy (E_a) of a solute is provided in Figure 2. Here, the term 'site energy' refers to the energy of a solute atom that arises from its relative position in the local chemical environment. In the figure, the local composition and solute pairings within the first two nearest neighbor shells (ζ) in a FCC lattice have been systematically varied for a binary FeNi system using the EAM potential of Bonny et al. [40]. In consideration of the statistical distributions shown in Figure 1, each of these local arrangements is possible in a randomly arranged solid solution, albeit with differing probabilities. As shown in Figure 2, the change in E_a for a Ni atom varies with the sample composition (\bar{c}^{Ni} , Figure 2a), and with the partitioning of solute between the first (\bar{c}^{Ni}_1 , Figure 2b) and second nearest neighbor shells. The changes in E_a can be significant - reaching as high as ~165 meV/atom in some configurations. It is this observation of the connection between solute arrangement and the site energy that informs our approach to predicting the statistics of fluctuations.

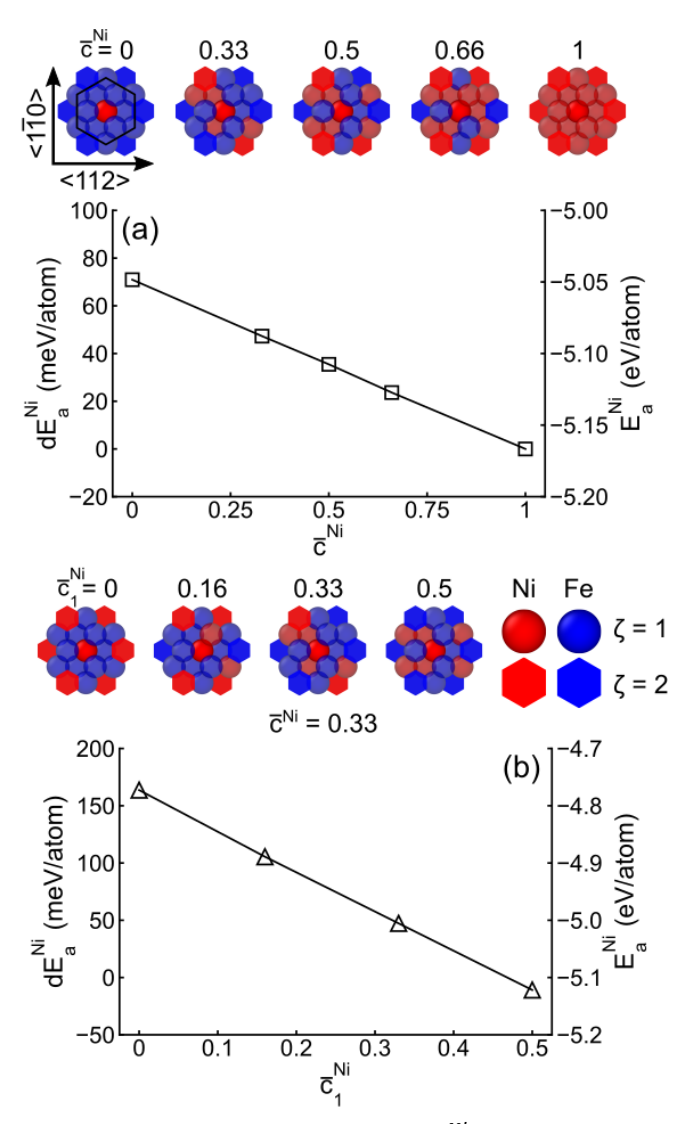


Figure 2: The change in per atom site energy of a Ni atom (dE_a^{Ni}) within the FCC phase of a FeNi solution. The overall sample composition (\bar{c}^{Ni}) is varied in (a) with an equi-proportional partitioning of solute between each neighbour shell (ζ) . The composition of the first neighbour shell (\bar{c}_1^{Ni}) is varied in (b) at an overall sample composition of $\bar{c}^{Ni} = 0.33$. The central Ni atom is not included in composition measurements. The right axis plots the nominal energy of the Ni atom (E_a^{Ni}) . Here, the PE zero-point is selected at the infinite separation of atoms. For presentation simplicity, energies are calculated from interactions up to 2 nearest neighbor shells only and are referenced relative to a pure Ni sample. The distribution of solute for each sample is illustrated in the schematics above each plot. The schematics are drawn from a <111> zone axis and atoms coplanar with the central Ni atom are marked by a black hexagon for clarity. Circular and hexagonal atom markers indicate solute in the first and second neighbor shells, respectively.

2.1. Statistical analysis in the embedded-atom method

The key to our approach to analyze PE fluctuations lies in recasting the equations of the interatomic potential in terms of the coordination environment around an atom such that varied compositions and neighbor pairings may be considered. To quantify these PE landscape

fluctuations in the statistical average and standard deviation are of interest. The inspiration for our approach follows from Varvenne et al. [28], where solute effects are treated through the creation of an EAM-based average-atom interatomic potential, which enables estimates of the homogenized properties of the bulk. Under the EAM, the PE of a system (E) is defined by the addition of two terms. The first term is the embedding energy (F), which is a function of the charge density (ρ) contributed by neighboring atoms at distance r. The second term is the interaction energy (V) that captures the pairwise potential energy interactions between atoms. In their usual presentation, the EAM terms are summed over all atom sites and element types. This summation can be directed by binary occupancy vectors C_i^X (as in Appendix A), which return $C_i^X = 1$ when an atom of type X occupies site i and are otherwise 0. The total PE of the system can then be calculated as [28-31]:

$$E = \sum_{i,X} C_i^X F^X(\rho_i) + \frac{1}{2} \sum_{i,j \neq i,X,Y} V_{ij}^{XY} C_i^X C_j^Y$$
 (1)

with the indices *ij* and *XY* specifying the atomic and chemical pairs, respectively. Using the occupancy vector, the charge density under the EAM is given as:

$$\rho_i = \sum_{i \neq i, X} C_j^X \rho_{ij}^X \tag{2}$$

For the purposes of this study, we are interested in determining the per atom PE using similar relations. To achieve a per atom description, we reparametrize these relations through the introduction of the coordination number (N_{ζ}) , which provides the number of atoms in concentric shells at fixed distances from a central atom. For instance, N_1 takes on a value of 12 for the nearest neighbors in FCC materials. These concentric shells of coordination are a

superset of the nearest neighbor shells described above and are incremented with increasing radial distance. As demonstrated in the upcoming discussion, this relatively simple modification allows for the statistics of varied local solute environments to be analyzed. Moreover, this reparameterization can be leveraged to study a variety of PE landscapes, provided the coordination relations are known. This information is readily available for perfect crystals, which directly delivers the statistics of the cohesive energy landscape and can be obtained for some crystal defects such as FCC planar faults. This process is demonstrated in Section 2.2, where relations for the statistics of a varied GPFE landscape in a FCC system are provided. While this approach implicitly neglects lattice distortion effects on statistical parameters, results show that this assumption is reasonable for the systems studied herein.

The statistical analysis begins with an examination of the average per atom energy in a multicomponent system through summation of the reparametrized EAM relations over all element types and coordination shells. Under the assumption of a random arrangement of solute, the average per atom site energy (\bar{E}_a) can be calculated as:

$$\bar{E}_a = \sum_X \bar{C}^X F^X(\rho) + \frac{1}{2} \sum_{X,Y,\zeta} V_\zeta^{XY} N_\zeta \bar{C}^X \bar{C}^Y$$
(3)

where \bar{C}^X is the average concentration of a solute as defined previously. Here, V_ζ^{XY} represents the pair interaction energies of solutes at distances corresponding to the various coordination shells, which are available directly from the interatomic potential. In this work, the summation of coordination shells is restricted by a cutoff distance. This cutoff distance was chosen to be the same as those specified in the EAM potential used in validation activities (see

Section 3). In all materials studied the cutoff distances is no less than $\sqrt{5}/2 a_o$, where a_o is the lattice parameter (here, $a_o \approx 0.35$ nm). This results in a summation of at least the first five coordination shells in all crystals considered, which was found to surpass any cutoff sensitivity. Following the assumption of Varvenne et al. [28], the per atom charge density term, ρ , is replaced with an average per atom charge density ($\bar{\rho}$). This replacement simplifies the statistical analysis and is found to retain excellent accuracy for the systems studied in this work. For instance, using the systems studied in Section 3.2 as a benchmark, this approximation resulted in deviations of less than 0.3% to average per atom embedding energies (\bar{F} , see Eq. (5)), when compared against exact calculations. The average per atom charge density follows as:

$$\bar{\rho} = \sum_{X,\zeta} \rho_{\zeta}^{X} \bar{C}^{X} N_{\zeta} \tag{4}$$

where ρ_{ζ}^{X} represents the charge density contributed by solute X in coordination shell ζ , and is provided by the interatomic potential. In Eqs. (3) and (4), the average concentrations offer the weighted probabilities of finding solute X in coordination shell ζ for each term in the EAM relations.

Within the context of previous work, the relations provided in Eqs. (3) and (4) can be viewed as per atom analogs to the system-level homogenized relations developed in Varvenne et al. [28]. Analysis of the statistical scatter in per atom energies proceeds from separate calculations of the standard deviations of the embedding energies (ΔF) and pair interaction energy terms (ΔV). Under the constant charge density assumption, the standard deviation of the embedding energy is given as:

$$\Delta F = \sqrt{\sum_{X} (F^X - \bar{F})^2 \bar{C}^X}$$
 (5)

where F^X is the embedding energy of element X evaluated at $\bar{\rho}$, and $\bar{F} = \sum_X F^X \bar{C}^X$ is the average per atom embedding energy. This expression for ΔF may be interpreted as a weighted combination of the variances of individual solute embedding energies.

Due to the varied pair interactions between different solutes in coordination shells, analysis of the standard deviation of the pair interaction energy term requires a systematic approach that considers each pairing that contributes to statistical scatter. As demonstrated in Figure 1, the local concentration in the vicinity of a solute atom may vary significantly from the global chemistry, and the partitioning of solute into differing coordination shells (see Figure 2) presents additional pathways for statistical scatter. These added considerations underscore the complexities that arise in determining the PE statistics of solid solutions. The final relation for the standard deviation of the pair interaction energy is given as:

$$\Delta V = \sqrt{\sum_{X} \bar{C}^{X} (\Delta V^{X})^{2} + \sum_{X < Y} \bar{C}^{X} \bar{C}^{Y} (\bar{V}^{X} - \bar{V}^{Y})^{2}}$$
 (6)

where \bar{V}^X and ΔV^X are the average and standard deviations of the per atom interaction energies, respectively, when solute X is the central atom. These terms can be separately calculated from the parameters of EAM potentials as:

$$\bar{V}^X = \sum_{\zeta, Y} V_{\zeta}^{XY} \bar{C}^Y N_{\zeta} \tag{7}$$

$$\Delta V^X = \sqrt{\sum_{\zeta,Y} \left(V_{\zeta}^{XY} - \bar{V}_{\zeta}^X\right)^2 \bar{C}^Y N_{\zeta}}$$
(8)

where $\bar{V}_{\zeta}^{X} = \sum_{Y} V_{\zeta}^{XY} \bar{C}^{Y}$ is the average interaction energy for a solute X in coordination shell ζ . A detailed derivation of ΔV and the related terms is provided in Appendix B. Using the standard rules for the combinations of statistical variables, Eqs. (5) and (6) may be combined to provide the standard deviation of the per atom energy (ΔE_a):

$$\Delta E_a = \sqrt{\Delta F^2 + \left(\frac{\Delta V}{2}\right)^2 + 2cov\left(F, \frac{1}{2}V\right)} \tag{9}$$

where $cov\left(F,\frac{1}{2}V\right)$ is the covariance between the embedding and the pair interaction energies. The $^{1}/_{2}$ coefficient appears in the ΔV and covariance terms to avoid double counting of interaction energies, as in Eq. (1). The covariance term can be calculated directly from the overall composition and the interatomic potential coefficients as:

$$cov\left(F, \frac{1}{2}V\right) = \frac{1}{2} \sum_{X} \bar{C}^{X} F^{X} \bar{V}^{X} - \left(\sum_{X} \bar{C}^{X} F^{X}\right) \left(\frac{1}{2} \sum_{X,Y,\zeta} V_{\zeta}^{XY} N_{\zeta} \bar{C}^{X} \bar{C}^{Y}\right)$$
(10)

A full derivation of this expression is provided in Appendix C.

Collectively, Eqs. (3) - (10) provide a method to evaluate the statistical variations of per atom potential energies in randomly arranged solid solutions. These relations are derived directly from the EAM formulation and require only coefficients from the interatomic potential, solute concentrations, and coordination relations as inputs. Furthermore, there are no adjustable parameters or new assumptions introduced to produce these statistical relations. These equations are general and can be applied to any crystalline structure, provided the coordination relations are given. Indeed, the application of these relations to planar faults is a necessary step

in the analysis of the GPFE landscape that follows in the next section.

2.2. Extension of per atom EAM relations to the GPFE landscape

The PE landscapes considered in this study are those of the cohesive energy and the GPFE. The cohesive energy landscape is a composite of per atom site energy values that describe the potential energy change due to deposition from the gas phase into a crystalline phase, which serves as a reference for comparison of phase stability. The statistical parameters of the cohesive energy landscape can be therefore retrieved directly from Eqs. (3) - (10). The GPFE landscape is formed from the area normalized interplanar excess energy (i.e., the planar fault energy, γ [41,42]) arising from the coordinated shearing of the pristine FCC lattice by Shockley partial dislocations along <112>/{111}, as required to form and thicken deformation twins. Within the context of deformation mechanisms, the GPFE landscape can be used to examine the intrinsic competition between dislocation slip and deformation twinning in a FCC material, which has important implications on the evolution of mesoscale plasticity in low stacking fault energy systems. The tendency for a material to exhibit deformation twinning is described through a variety of twinnability parameters [43-49], which are dependent on the critical energies (i.e., peaks and valleys) of the GPFE landscape. Figure 3 provides a schematic of a typical GPFE landscape for an FCC material, with the critical energies labeled. These energies are the unstable stacking fault energies ($\gamma_{usf}^{0.5}$ and $\gamma_{usf}^{1.5}$), the intrinsic and extrinsic stacking fault energies (γ_{isf}^1 and γ_{esf}^2), and the unstable twinning and twinning fault energies $(\gamma_{utf}^{2.5})$ and γ_{tf}^{3} . Here, the superscript refers to the crystallographic slip that is required to create each fault, referenced as a multiple of the <112> Shockley partial Burger's vector (b₁₁₂). Fluctuations in these critical energies are of interest to the community, as they have implications on deformation mechanism competition [43–46,48,49], the waviness of stacking faults ribbons [8,36], variations in twinning stresses [50], and the local stability of FCC and HCP phases [51,52], amongst other elements of mechanical metallurgy.

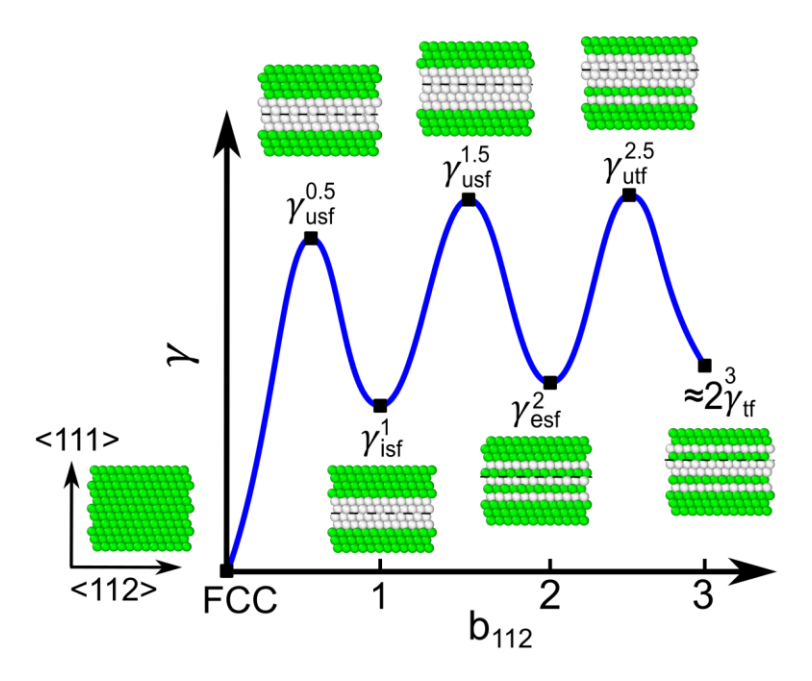


Figure 3: A schematic of the GPFE landscape that is formed from the interplanar excess energy of a FCC crystal. To form this curve, the crystal is sequentially sheared along <112> in consecutive {111} planes, as specified by the deformation twinning formation pathway. Shearing is measured here in increments of the <112> Shockley partial Burger's vector (b_{112}). The critical energies of the GPFE landscape are indicated. γ_{tf}^3 is normally calculated from an isolated planar fault and is approximately equal to half the twin fault configuration shown here [47]. Snapshots of the idealized atom configurations in the vicinity of each fault are provided. Green and white atoms are classified as FCC and non-FCC coordinated, respectively. A discussion of this classification procedure is provided in the main text. Dashed lines separate the {111} crystallographic planes involved in the progressive shearing of the FCC crystal.

Analysis of the fluctuations in the critical energies of the GPFE begins with the recognition that the configuration of solute around each of the associated planar faults can be fully described by sets of coordination relations. Therefore, the statistical relations of the previous section can be leveraged to analyze fluctuations in the local minima and maxima of the GPFE landscape. However, in contrast to the pristine FCC lattice, where relations are spatially invariant, the coordination environment changes for atoms lying in each of the {111}

crystallographic planes near a planar fault due to changes in the local stacking sequence. Figure 4 illustrates the changes in the coordination relations in the {111} layers near an unstable stacking fault for a cutoff of $\sqrt{\frac{5}{2}}a_o$. Coordination relations for larger cutoffs appear similar, but with more non-FCC layers and peaks. Here, we use a two-index notation (n, m) to refer to faulted planes, where n refers to the number of Shockley partial dislocations required to create the defect, and m is a $\{111\}$ layer enumerated sequentially from the shearing interface (m = 0). As shown in Figure 4, the disruption of the normal stacking sequence gives rise to new peaks in the coordination relations. Intuitively, the appearance of non-FCC peaks occurs at larger radial distances in layers further from the shearing interface, until they are pushed outside of the cutoff radius (i.e., $\sqrt{\frac{5}{2}}a_o$). In classifying FCC and non-FCC coordinated crystallographic layers, a comparison of coordination relations within the cutoff radius is used as the guiding criterion. Other schemes (e.g., based on stacking sequence) may lead to different classifications. Coordination relations for the other interplanar defects associated with the critical energies of the GPFE landscape (i.e., the unstable stacking and twinning faults, extrinsic stacking fault, and twin fault) are provided in the Supplementary Materials, Figures S1-S5. The non-FCC coordinated planes used in the statistical analysis of each critical energy of the GPFE landscape are provided in Table 1. It should be noted that the location of m = 0 is not the same for each planar fault due to the sequencing of plane shearing required to create each defect.

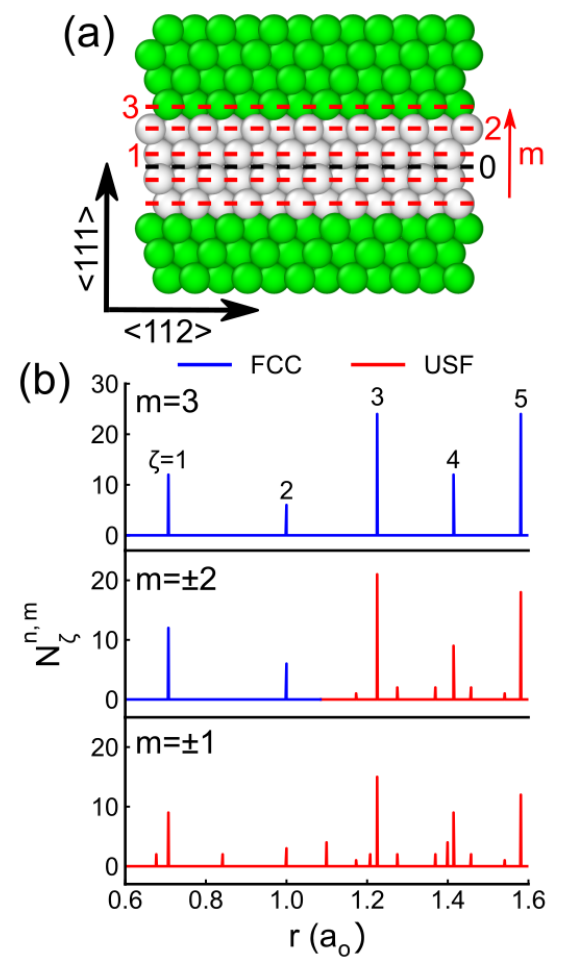


Figure 4: (a) The idealized configuration of atoms in the vicinity of an unstable stacking fault (USF) viewed from a <110> axis. The traces of {111} crystallographic planes (red dashed lines) are enumerated sequentially from the shearing interface (m = 0, black dashed line). Green and white atoms are classified as FCC and non-FCC coordinated, respectively. A discussion of this classification procedure is provided in the main text. (b) The idealized coordination relations are shown for atoms in {111} layers near the unstable stacking fault $\left(N_{\zeta}^{n,m} = N_{\zeta}^{0.5,m}\right)$. Additional coordination peaks are seen in layers adjacent to the shearing interface. The coordination relations return to the FCC sequencing at m = 3, as the additional coordination peaks are pushed beyond the cutoff radius. Peaks that differ in position or magnitude to the FCC coordination (blue) are colored in red. ζ is the index used to enumerate these peaks in statistical relations. An example of this process is provided for the FCC coordination (m = 3). Coordination relations are plotted against distance (r) in multiples of the lattice parameter as the radial position of ζ varies by defect type and {111} crystallographic plane.

Calculation of the average planar fault energy $(\bar{\gamma})$ follows directly from a comparison of average per atom energies in the faulted and fault-free conditions as:

$$\bar{\gamma}^n = \rho_{111} \sum_m (\bar{E}_a^{n,m} - \bar{E}_a^{FCC})$$
 (11)

where $ar{\it E}_a^{\it FCC}$ and $ar{\it E}_a^{\it n,m}$ are the average per atom energies for an FCC coordination and the

coordination in the m^{th} {111} layer near a n-type fault, respectively. ρ_{111} is the number density of atoms in the FCC {111} plane, which is given as $4/\sqrt{3}a_0^2$. \bar{E}_a^{FCC} can be calculated directly from Eq. (3). Determination of $\bar{E}_a^{n,m}$ follows from a separate application of Eq. (3) to each of the coordination environments in the m layers around a planar defect (see Figure 4), with $F^X = F^{X,n,m}$, $V_\zeta^{XY} = V_\zeta^{XY,n,m}$, and $N_\zeta = N_\zeta^{n,m}$. The latter terms $(V_\zeta^{XY,n,m}$ and $N_\zeta^{n,m}$) are given directly by the interatomic potential and topology, respectively, and $F^{X,n,m}$ is calculated from the relevant terms of Eqs. (4) and (5) evaluated under the faulted coordination relations.

Table 1: Non-FCC coordinated planes in the vicinity of the critical planar faults of the GPFE landscape.

Planar Fault Energy (n)	Total layers (M)	Non-FCC planes (m)
$\gamma_{usf}^{0.5}$	4	±1, ±2
γ_{isf}^1	4	$\pm 1, \pm 2$
$\gamma_{usf}^{1.5}$	5	$-3, \pm 1, \pm 2$
γ_{esf}^2	3	-3, -1, 2
$\gamma_{utf}^{2.5}$	5	$-4, \pm 1, \pm 2$
γ_{tf}^3	4	$-4, -1, \pm 2$

Calculation of the standard deviation of the planar fault energy ($\Delta \gamma$) begins with a determination of the standard deviations of per atom energies in each of the m {111} crystallographic layers influenced by a n-type fault (i.e., $\Delta E_a^{n,m}$). For standard deviation calculations, we consider only those {111} layers whose coordination relations differ from the pristine FCC case within the specified cutoff radius to avoid the convolution of cohesive energy and excess energy distributions. The $\Delta E_a^{n,m}$ terms can be retrieved through the application of Eqs. (3)-(10) in Section 2.1 using the same modifications to the embedding and pair interaction energies and coordination relations as in the calculation of $\bar{E}_a^{n,m}$. Using the same rationale for calculating the aggregated statistics of non-overlapping sub-populations in per atom interaction energies (see Eq. (6) and Appendix B), the standard deviation of faulted per atom energies

 (ΔE_a^n) over all non-FCC layers in the vicinity of a planar fault is calculated as:

$$\Delta E_a^n = \sqrt{\frac{1}{M} \left[\sum_m (\Delta E_a^{n,m})^2 + \frac{1}{M} \sum_{m1 < m2} (\bar{E}_a^{n,m1} - \bar{E}_a^{n,m2})^2 \right]}$$
(12)

where M is the total number of non-FCC coordinated layers created by the planar fault. Following the rules for the addition and subtraction of statistical variables, we arrive at a relation for the standard deviation of the planar fault energy ($\Delta \gamma$), which can be calculated from the sum of variances in the faulted and fault-free conditions:

$$\Delta \gamma^n = \sqrt{(\Delta E_a^n)^2 + (\Delta E_a^{FCC})^2 - 2cov(E_a^n, E_a^{FCC})} \,\rho_{111} \tag{13}$$

where $cov(E_a^n, E_a^{FCC})$ is the covariance between faulted and non-faulted per atom energy distributions, and ρ_{111} is the planar number density as defined in Eq. (11). The covariance between these distributions can be determined from the difference between the expectation value of products and the product of expectation values. We find a good approximation to this exact definition from the following relation:

$$cov(E_a^n, E_a^{FCC}) \approx \frac{1}{M} \left(\sum_{X,m} \bar{C}^X \bar{E}_a^{X,n,m} \bar{E}_a^{X,FCC} - \bar{E}_a^{FCC} \sum_m \bar{E}_a^{n,m} \right)$$
(14)

where $\bar{E}_a^{X,n,m}$ and $\bar{E}_a^{X,FCC}$ are the solute-level average per atom energies in the faulted and FCC-coordinated conditions. These terms may be calculated as:

$$\bar{E}_a^{X,n,m} = F^{X,n,m} + \frac{1}{2}\bar{V}^{X,n,m} \tag{15}$$

$$\bar{E}_a^{X,FCC} = F^{X,FCC} + \frac{1}{2}\bar{V}^{X,FCC} \tag{16}$$

with the \bar{V}^X term given by Eq. (7) evaluated in the corresponding coordination environment. A detailed derivation of $cov(E_a^n, E_a^{FCC})$ and the associated parameters is provided in Appendix C.

The analysis presented in Sections 2.1 and 2.2 provides a method to calculate the statistics of fluctuations in the cohesive energy and GPFE landscapes. These relations are derived for EAM-type interatomic potentials, which are relevant for metals and alloys, and can be applied to systems of arbitrary components and compositions. While this method is general across a variety of material systems, one limitation is that the coordination relations must be fixed by symmetry either in a crystal lattice (i.e., as in the cohesive energy landscape) or within a faulted plane (i.e., as in the GPFE landscape). PE landscapes that are not captured by these conditions require additional derivations. Caution must also be exercised in the interpretation of results, as the physical relevance of the statistical analysis is limited by the accuracy of the underlying EAM potential, which have known limitations in systems with strong angular-dependent interactions [53]. Nonetheless, the relatively simple form of these relations enables scripting in algorithms for rapid computation. Python-based codes to calculate the statistical parameters of cohesive energy and GPFE landscapes for randomly arranged solid solutions are available at an online repository managed by the authors [54]. In subsequent sections, results and validation datasets are presented for the cohesive energy and GPFE landscapes in the NiCo and FeNiCr systems.

3. COMPARISON TO DIRECT MS SIMULATIONS

The statistical relations developed in previous sections are validated using molecular statics

(MS) simulations with the Large-scale Atomic/Molecular Massively Parallel Simulator (LAMMPS) software package [55]. Visualization of simulation topologies is realized using The Open Visualization Tool (OVITO) [56]. Two simulations are performed: simple MS relaxation calculations and interplanar shearing simulations, which are used to validate predictions of fluctuations in the cohesive energy and GPFE landscapes, respectively. The procedures for these simulations are well established within the community (e.g., Refs. [2,14– 16,28,34]). Data presented in the main text corresponds to systems measuring at least 10 by 10 by 5 nm (> 50,000 atoms) and 35 by 35 by 7 nm (> 800,000 atoms) in size for MS relaxation and interplanar shearing simulations, respectively. System sizes are chosen based on convergence studies, with the average values of cohesive and planar fault energies used as convergence criteria. For instance, GPFE convergence studies in the Fe₇₃Ni₈Cr₁₉ system showed deviations in average fault energies of less than 7 mJ/m² (with most deviations less than 2 mJ/m²) in simulation cells larger than 10 x 10 nm in the lateral dimension and 3 nm in height (see Supplementary Materials, Figure S6). MS relaxation calculations are performed using the conjugate gradient minimization tool built within LAMMPS. Simulation boundaries are periodic in all directions and are allowed to expand/contract to minimize stresses. For interplanar shearing simulations, we have followed the same methodology from our previous work [47]. Briefly, single-crystal FCC systems are constructed such that the <110>, <112>, and <111> crystallographic directions are aligned to the global x, y, and z axes, respectively. Periodic boundary conditions are enforced on the x and y boundaries and the z surfaces are free surfaces. The GPFE curve is obtained through a three-stage rigid shearing process, where the shear per stage is equal to the magnitude of a <112>-type Shockley partial dislocation (i.e., $\frac{a_o}{\sqrt{6}}$). This shearing process begins its first stage by displacing two halves of the crystal along the <112> direction within a {111} shear plane. The second and third stages are completed by shearing the crystal at the plane immediately adjacent to the fault formed in the prior stage, as required to realize a twin fault. Each shearing stage is executed over 100 shearing increments to capture the intermediate configurations and excess energies of the GPFE landscape. In between each shearing step, the system is relaxed in the z-direction and the per atom potential energies are recorded. The GPFE is then obtained from the per atom energies of the relaxed configurations (i.e., the distribution E_a). The average planar fault energy (i.e., $\bar{\gamma}$) can be directly calculated over the faulted layers using the relation in Eq. (11). In MS simulations, the standard deviation of planar fault energies (i.e., Δy) is determined from its definition as the expectation value of deviations from the mean: $\Delta \gamma = \sqrt{\langle ([E_a^n - \bar{E}_a^n] - [E_a^{FCC} - \bar{E}_a^{FCC}])^2 \rangle} \rho_{111}$, where () refers to the expectation value operator. The standard deviation is calculated here from non-FCC {111} layers using the same cutoff criteria as described in Section 2.2.

3.1. Concentrated solid solution system selection

For the purposes of this study, we have selected the binary NiCo and ternary FeNiCr systems as our benchmark materials. One key selection criteria for these systems is their relevance in deformation twin [57–59] and stress-induced HCP martensite forming materials [59–62], for which the fluctuations in the fault energies of the GPFE landscape are of inherent interest. In addition to these characteristics, the FeNiCr system is selected due to its technological importance in stainless steels and the availability of computational datasets from which results may be validated [28,32,33,63,64]. The NiCo system also offers the opportunity

to study the accuracy of our method in polymorphic solid solutions, with a FCC to HCP transition known in this system at ~ 70 at.% Co [65]. The following sections present the application of the equations of Sections 2.1 and 2.2 to the FeNiCr and NiCo systems over a wide compositional range. Although the FeNiCr system exhibits complicated multiphase microstructures at some compositions, our analysis focuses on the FCC structure as a theoretical exercise. Validation datasets have been generated from MS relaxation studies using the procedures described above. For these simulations, the EAM-based potentials of Bonny et al. [40] (FeNiCr) and Béland et al. [66] (NiCo) are used to model interatomic interactions. The cutoff radii used in the MS simulations and statistical analysis of FeNiCr and NiCo are 0.56 and 0.65 nm. Using the compositions of Section 3.2 as benchmark systems, the zero Kelvin FCC lattice parameters were measured in the ranges of 0.352 – 0.356 nm (Ni_{1-x}Co_x) and 0.349 – 0.358 nm (Fe(1-x)/2Ni(1-x)/2Cr_x).

3.2. Statistical analysis of the cohesive energy landscape

The statistical parameters of the cohesive energy landscape are given directly by the average and standard deviations of per atom site energies (i.e., \bar{E}_a and ΔE_a). Figure 5 provides these quantities for the FCC phase of the FeNiCr, and the FCC and HCP phases of NiCo. The FeNiCr compositional space is charted along a search path of Fe_{(1-x)/2}Ni_{(1-x)/2}Cr_x, with literature data provided from Ref. [28] for validation purposes. Results are obtained for NiCo across its entire compositional space. Using the statistical relations of Section 2.1, analytical calculations are displayed alongside the results of MS relaxation simulations. As shown in the figure, \bar{E}_a is shown to vary monotonically from ~ -4.5 to -3.7 eV/atom for the FeNiCr data. The NiCo system exhibits ranges of ~ -4.45 to -4.38 and ~ -4.43 to -4.39 eV/atom

for the FCC and HCP phases, respectively. MS relaxation data show excellent agreement with the predictions of the statistical relations for both systems. Indeed, the analytical estimates of per atom average energies deviate by less than 0.5% for both FeNiCr and NiCo. Furthermore, the statistical relations accurately capture the transition in FCC to HCP phase stability at Corich compositions of > 70 at.%.

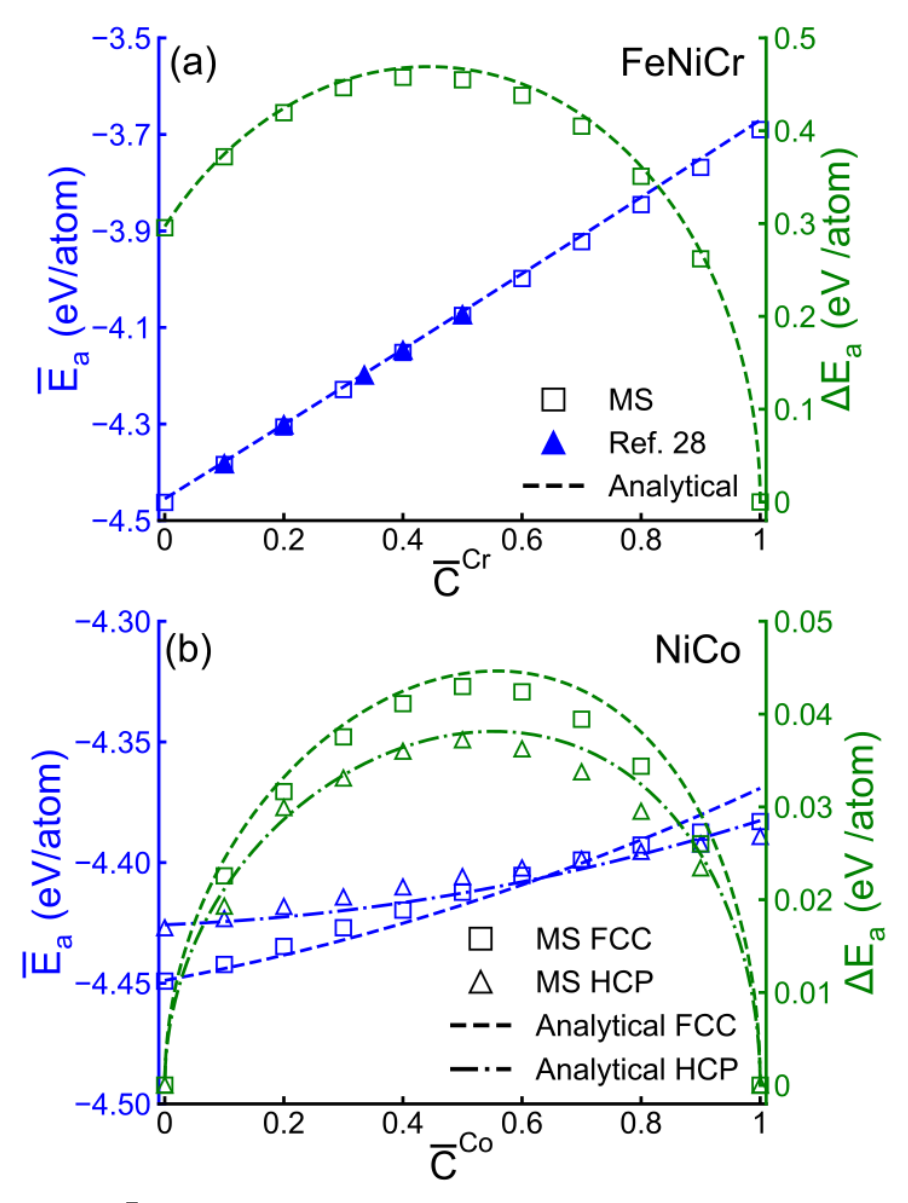


Figure 5: The average (\bar{E}_a) and standard deviations (ΔE_a) of per atom site energies in the (a) Fe_{(1-x)/2}Ni_{(1-x)/2}Cr_x and (b) NiCo systems. Predictions from the statistical relations (Analytical) are overlaid with data from MS relaxation simulations, showing excellent agreement. Cohesive energy data from Varvenne et al. [28] are also provided for the FeNiCr system. The average energies and standard deviations are plotted against the primary (blue) and secondary axes (green), respectively.

Standard deviations in the per atom energies were found to vary between 0 to ~0.46 eV/atom and 0 to ~ 0.043 eV/atom across the sampled FeNiCr and NiCo systems, respectively. The large standard deviations in FeNiCr datasets are driven by the dramatic change in per atom energies with increasing Cr content. Conversely, NiCo per atom energies vary only slightly across its compositional space, which leads to lower standard deviations. As with the average per atom energies, the standard deviations in the MS data show excellent agreement with analytical calculations. Indeed, deviations in analytical estimates of standard deviations are < 5% for both FeNiCr and NiCo, except at singularities near the terminal compositions where the standard deviations approach zero. Comparison between datasets shows that these analytical relations accurately capture the order of magnitude changes in statistical fluctuations across different systems and chemistries. Some features of this agreement bear noting. Namely, the statistical relations accurately predict a vanishing standard deviation at pure chemistries (i.e., right of FeNiCr plot and terminuses of the NiCo plot). Furthermore, our statistical relations also capture the asymmetry in the standard deviation of the NiCo system. More broadly, the strong agreement between our idealized analytical approach and relaxed MS datasets demonstrates the importance of the distribution of solute arrangements in driving PE fluctuations. Moreover, these results also indicate that lattice distortion effects hold a minor role in the determination of per atom energy statistics. To contextualize this interpretation, we have quantified the lattice distortion of the equimolar FeNiCr and NiCo systems using the atomic size difference parameter (δ) [67,68]. This parameter is calculated as: δ = $\sqrt{\sum_X \bar{C}^X (1 - r^X/\bar{r})}$, where r^X is the atomic radius of the solute and $\bar{r} = \sum_X \bar{C}^X r^X$ is the average radius. Using data extracted from the radial distribution functions of FCC MS relaxation calculations on pure element systems, we obtain atomic size differences of 1.14% and 1.20% for FeNiCr and NiCo, respectively. For comparison, a similar calculation on the Cantor alloy (equimolar CrMnFeCoNi) produces an atomic size difference of 1.26%. One interpretation from these findings is that although lattice distortion certainly exists in these solid solutions, the energetic fluctuations induced by disruptions to the lattice on an atom-by-atom basis are self-reconciling. However, caution must be taken when generalizing this finding to other PE landscapes or systems with more pronounced mismatches in atoms size, where lattice distortion effects may exhibit a stronger effect on the emergence of relaxed energies.

In addition to insights into lattice distortion effects, these results provide new tools to quantify local phase stability, which contributes to the ongoing dialogue of metastable microstructures in concentrated solid solutions. For instance, recent studies of FCC equimolar CrCoNi have provided some conflicting results. Here, the intrinsic stacking fault energy, whose polarity can be taken as an indicator of FCC/HCP stability, finds a wide range of positive and negative values in the literature. Namely, density functional theory (DFT) studies of this system report energies between -24 to -62 mJ/m² [51,69–71], which contradicts experimental measurements of positive values for the stacking fault energy (~ 22 mJ/m²) [72,73]. Although there are several explanations for these discrepancies such as overlooked ordering effects [74] and drag on fault ribbons from strong solute/dislocation interactions [37], an alternative interpretation is that the varied chemical environment in low stacking fault energy FCC concentrated solid solutions possess regions where the HCP phase is favored due to fluctuations

in the FCC/HCP cohesive energies. This interpretation aligns with the work of Zhao et al. [17], which demonstrated strong size effects in DFT calculations of the stacking fault energies of NiCo and CrCoNi. In both materials, a distribution of stacking fault energies is reported, with some positive and negative values being captured in the statistics. The results of this section add new quantitative tools to analyze this metastability argument. As demonstrated in the NiCo system, local variations in chemistry and solute pairings create sufficiently large statistical fluctuations in PE such that the FCC and HCP phases exhibit overlapping distributions of cohesive energies.

The success of our statistical relations in replicating the per atom energies of MS relaxation calculations motivates a computational search of compositional spaces without the need for exhaustive atomistic simulations. Figure 6 presents the statistical parameters of the cohesive energy landscape in ternary plot form for the entire compositional space of the FeNiCr system, with the compositions reported in Figure 5 traced with a dashed arrow. Some interesting features emerge from this complete search of the FeNiCr system. Namely, the largest standard deviations in the per atom energies are found along the binary NiCr terminus of this ternary diagram. This result may be understood from an examination of the per atom site energies in the FeNiCr system, which reach their minimum and maximum values at the pure Ni (\sim -4.5 eV/atom) and Cr (\sim -3.7 eV/atom) compositions, respectively. Consequently, to a first approximation, the standard deviation can be expected to reach a maximum at an equimolar chemistry of NiCr. We believe that this finding is consequential within the broader context of PE landscapes in solid solutions. For instance, recent theories have demonstrated the role of

large PE fluctuations in driving the unusual strengthening of HEAs. Examples include the solute-dislocation interaction model of Varvenne et al. [8,13] and the stochastic Peierls-based model of Zhang et al. [9]. The success of these theories, combined with the community's enthusiasm for HEAs, has led to perhaps an overly restrictive perspective on opportunities for property improvements. That is, increasing the number of components best realizes the benefits of solid solutions by maximizing solute dispersion. With some caveats, we offer this data as a theoretical counter example, where a binary sub-alloy exhibits larger PE fluctuations than a parent ternary. This finding aligns with the growing body of literature (e.g., Ref. [6]) that underscores the importance of solute interactions within the complex interplay between solute arrangement, number of components, and ensemble chemistry that define the contributions of solid solution effects in concentrated systems.

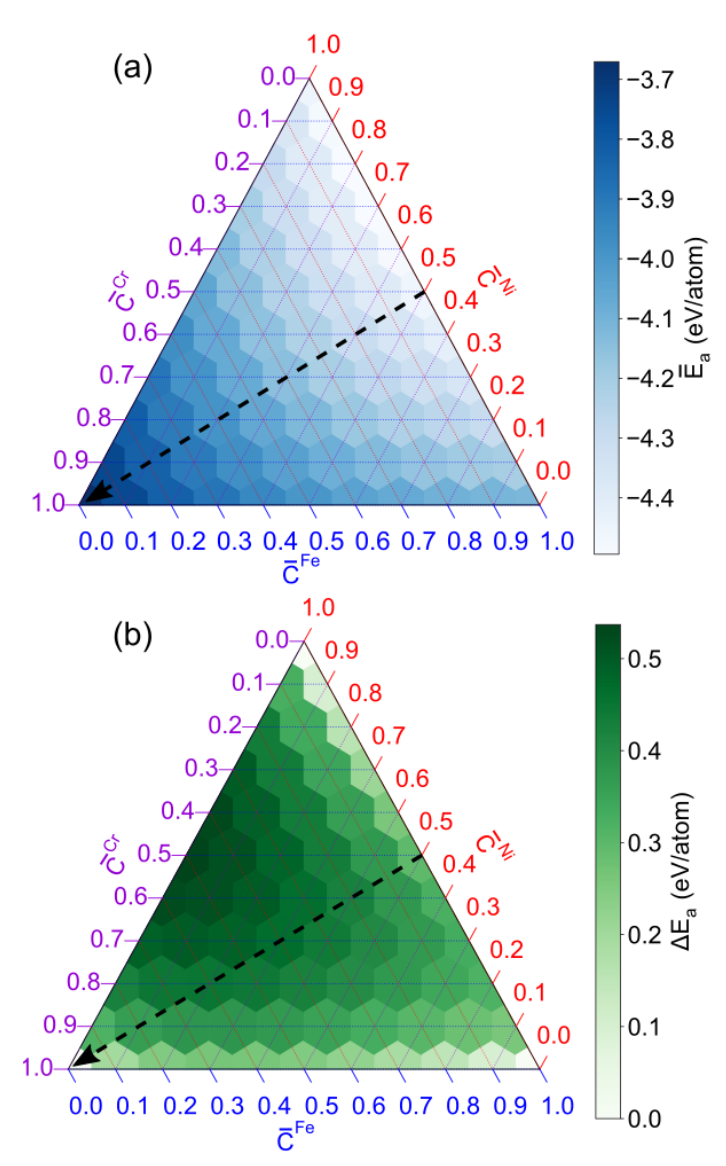


Figure 6: Ternary plots of the (a) average and (b) standard deviations of the per atom site energies in the FeNiCr system. All results are calculated using the statistical relations of Section 2.1. The dashed arrow traces the data presented in Figure 5. In this system, the largest standard deviations are found along the NiCr binary terminus of this plot, and not at the equimolar composition.

3.3. Statistical analysis of the GPFE landscape

Following the procedures outlined in Section 2.2, the standard deviations in the critical planar fault energies of the GPFE landscape have been studied for four different FCC solid solutions. The selected system chemistries are Fe₇₃Ni₈Cr₁₉, and equimolar FeNiCr, NiCr, and NiCo. The inclusion of NiCr is motivated by the peak statistical fluctuations observed at this chemistry in the cohesive energies of the previous section. Fe₇₃Ni₈Cr₁₉ has been selected due to its technological relevance in 304-type stainless steels, where deformation twinning is a

competing plasticity mechanism. As the first step in the determination of fault energies, Figure 7 provides the standard deviations of per atom energies at various faulted conditions for each of these systems. The data from MS shearing simulations is overlaid with predictions from statistical relations, showing excellent agreement. The largest deviations between datasets are found in the equimolar NiCo, but do not exceed 7% error, with most deviations being < 2%. Standard deviations range from between ~ 0.04 to 0.55 eV / atom, with the lower and upper extremes found in the equimolar NiCo and NiCr binary systems, respectively. These findings align with the cohesive energy data of pristine FCC systems, which showed similar ranges. Indeed, the introduction of planar faults was found to only change per atom energies by a maximum of $\sim 2\%$ in the FeNiCr chemistries and $\sim 6\%$ in equimolar NiCo. However, it should be noted that fluctuations in individual layers around a n-type fault may hold larger scatter than the aggregated variance of all M layers within the cutoff distance of the defect, from which ΔE_n^n is reported.

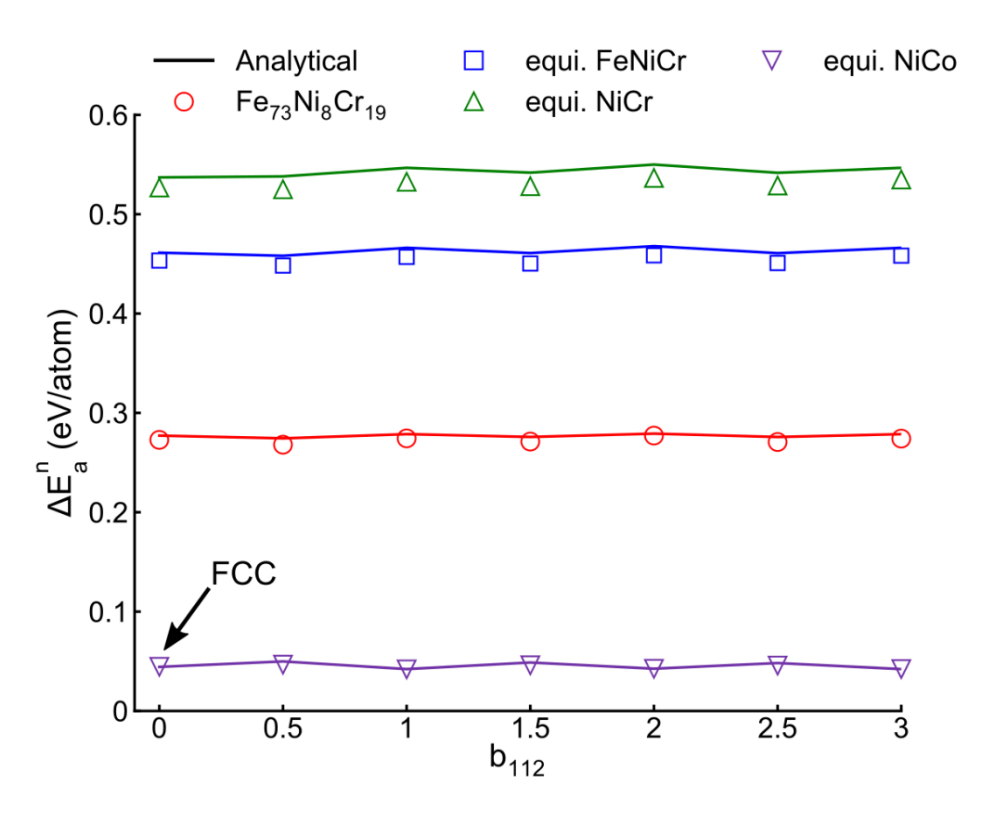


Figure 7: The standard deviation of per atom energies at various faulted conditions. This measurement includes contributions from {111} layers within the vicinity of planar faults. The FCC condition is shown at zero shear. MS shearing calculations are shown as markers and the predictions from statistical relations (Analytical) are overlaid in solid stroke.

Building upon the calculations of ΔE_a^n , we report the statistical scatter in the critical fault energies of the GPFE landscapes ($\Delta \gamma^n$) in Figure 8 for each system. The analytical calculations of $\Delta \gamma^n$ are shown as error bars and are overlaid with the GPFE landscapes calculated from interplanar shearing simulations. Literature values for the average intrinsic stacking fault energies in each system have been provided for comparison purposes. Some discontinuities in the GPFE landscape appeared at the stable planar faults, which we associate with changes in the numbers of non-FCC coordinated layers upon transitions through layer-by-layer shearing operations. For instance, upon formation of an extrinsic stacking fault, the m=1 plane exhibits a momentary FCC coordination (see Supplementary Material, Figure S3). This layer is therefore not included in the statistical analysis of the GPFE landscape, nor in the MS

simulations. However, MS simulations represent relaxed structures where some atoms in the m = 1 plane are in fact non-FCC coordinated and contribute to excess energy, but are no longer captured in the GPFE landscape calculation. This effect is most evident in the equimolar NiCr system and is negligible in others. The omission of these layers is required to remain directly comparable with the approach used in statistical analysis. That is, the determination of the standard deviations of fault energies in both approaches is sensitive to the number of atoms sampled. Therefore, to validate the accuracy of the statistical relations the same quantities must be inserted into the relations for MS and statistical estimates of the GPFE landscape. Furthermore, the inclusion of FCC-coordinated layers into the GPFE landscape statistics calculations convolutes the distribution of faulted per atom energies (i.e., E_a^n) with the cohesive energy landscape (i.e., E_a^{FCC}) natively present in these concentrated solid solutions, which creates ambiguity in the interpretation of standard deviations. In the bulk limit, the PE deviations caused by planar faults become negligible and statistics converge to the cohesive energy landscape values. To clarify the effect of {111} plane selection in the determination of the GPFE landscape from MS simulations, we have prepared a plot showing the effect of the number of {111} planes sampled on the average planar fault energies (see Supplementary Material, Figure S7), which demonstrates vanishing discontinuities.

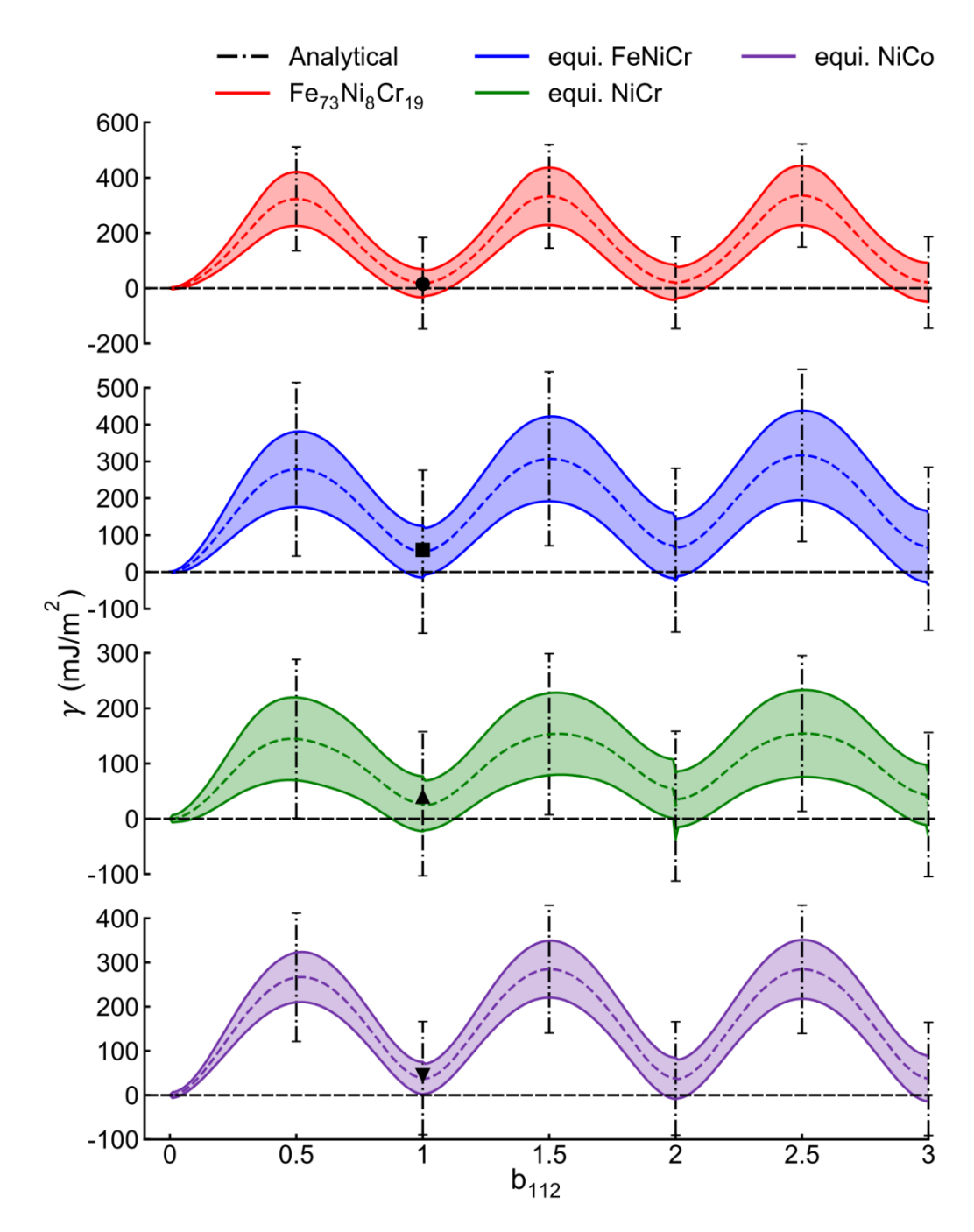


Figure 8: The GPFE landscapes of Fe₇₃Ni₈Cr₁₉ (a), equimolar FeNiCr (b), NiCr (c), and NiCo (d). Data from MS interplanar shearing simulations are provided in the colored stroke. The average planar fault energies appear as dashed lines and a region representing \pm 1 standard deviation is plotted as a filled curve bounded by solid lines. Analytical predictions for fluctuations in the critical fault energies are shown as error bars. A dashed line at $\gamma = 0$ is provided in each plot for readability purposes. Literature data on the average stacking fault energies of each system are provided as markers. This data is drawn from Refs. [17,28,40,75].

Although the analytical estimates of standard deviations exhibit only a modest agreement with the MS data, we find this result to be reasonable as the source of error is not related to any

new failings in our theory. Rather, these errors arise due to the nature of the standard deviation calculation in Eq. (13) and its extreme sensitivity to small changes in input parameters. Indeed, while analytical predictions for per atom energies and covariances (see Figure 7 and Figure C.1) are in excellent agreement with MS relaxation calculations, the subtractive elements of Eq. (13) greatly amplify any small discrepancies. The units of these fluctuations also provide useful context for consideration. That is, predictions of statistical scatter on the order of millipules over areas of squared meters would seem to be difficult to determine with great precision.

Despite only a modest numerical agreement between datasets, the trends and broader context of these results merit some discussion. In both approaches, the sequencing of the magnitudes of GPFE fluctuations are in agreement. Furthermore, both approaches predict that the NiCr system, which showed the highest fluctuations in cohesive energies, exhibits the lowest fluctuations in critical fault energies for each of the FeNiCr chemistries considered. This reduction in scatter is a result of the strong correlations observed in the NiCr system (see Figure C.1). An interesting interpretation of this result is that strongly correlated systems with large fluctuations in per atom site energies do not exhibit proportionally large fluctuations in their planar fault energies. An additional point of discussion from these results is the observations of fluctuations causing negative planar fault energies in both the analytical calculations and MS data. This is particularly relevant for the Fe₇₃Ni₈Cr₁₉ measurements as negative stacking fault energies are linked to the well-known stress-induced HCP martensite transformation exhibited by related stainless steel chemistries [59–62].

Within the broader context of concentrated solid solutions, we believe that the statistical relations developed in this work contribute to an ongoing discussion within the community on the interpretation of planar fault energies. For instance, recent studies of planar fault energies in medium- and high entropy alloys have reported a wide scatter in values [18,51,69,71]. Discussions in the newest literature have brought some clarity [36–39]. Namely, planar fault energies are sensitive to the arrangement of solute atoms near the fault plane, which gives rise to the concept of a "local" planar fault energy. Our results here offer a method by which the statistics of these local planar fault energies can be analytically studied. This contribution finds direct applications in quantifying the unusual metallurgy of concentrated solid solutions, with examples including waviness in stacking fault ribbons [8,36], and variations in solute-fault interaction energies [50].

4. CONCLUSIONS

An analytical approach has been developed to quantify the statistics of PE landscapes in randomly arranged solid solutions. For this purpose, the equations of EAM-based interatomic potentials are reparametrized to yield a set of relations defined by the coordination environment of solute. From these recast equations, exact relations for the statistical parameters of the embedding and pair interaction energy are derived. This set of initial relations is general and can be applied to study the cohesive energy landscapes of any crystalline system with an arbitrary number of components and composition. Using coordination as a key input parameter, we expanded the applicability of statistical relations to provide an analytical method to examine fluctuations in the excess energies of planar faults. Collectively, these analytical tools provide

the community a method to rapidly quantify PE fluctuations in pristine and defective solid solution systems described by sets of coordination relations, which finds applications in studies of local phase stability, and competition between deformation mechanisms.

In the second portion of this study, these relations are leveraged to study the cohesive energy and GPFE landscapes of FeNiCr and NiCo. In most cases, predictions from statistical relations were in excellent agreement with validation datasets that were collected from MS relaxation and interplanar shearing simulations. From this effort, some key insights into the metallurgy of solid solutions have emerged that contribute to ongoing discussions within the community. For instance, our results for NiCo offer a nuanced perspective on phase stability. That is, local variations in composition and solute pairings create sufficiently large fluctuations in cohesive energy that competing lattices find regions of favorable/unfavorable stability across a system topology. Within the context of the role of PE fluctuations in the physical properties of solid solutions, results from a theoretical search of the FeNiCr composition space contribute to a building theme in the literature. Namely, maximizing the effects of solid solution ensembles is more nuanced than simply selecting chemistries with the greatest solute dispersion. An additional outcome of this effort is a method to quantify the statistics of local planar fault energies, which is a new concept that has emerged from the varied stacking fault energies reported in the recent HEA literature.

APPENDIX A: DERIVATION OF COMPOSITION AND SOLUTE PAIR DISTRIBUTIONS

Following the method of Varvenne et al. [28], a multicomponent topology can be described by a set of binary occupancy vectors, C_i^X , which take on a value 1 if a solute of type X is

found at site i and are otherwise 0. Here, 'site' refers to the atomic positions that solute X would occupy in a crystal. The distribution of compositions collected by random sampling of n_c solute atoms from C_i^X is Gaussian with an average of \bar{C}^X . The average composition of individual samples is \bar{c}^X . The standard deviation of the solute ensemble (i.e., the population standard deviation, ΔC^X) can be determined directly from its definition:

$$\Delta C^X = \sqrt{\frac{\sum (C_i^X - \bar{C}^X)^2}{N}}$$
 (A.1)

where N is the length of the vector C_i^X . As the entries of C_i^X are binary, the numerator can be simplified to:

$$\Delta C^{X} = \sqrt{\frac{N^{X}(1 - \bar{C}^{X})^{2} + (N - N^{X})\bar{C}^{X^{2}}}{N}}$$
(A.2)

where $N^X = \sum C_i^X$. The ratio N^X/N is the population average, \bar{C}^X , by definition. Recognition of this relationship leads to a compact expression for the standard deviation as:

$$\Delta C^X = \sqrt{\bar{C}^X (1 - \bar{C}^X)} \tag{A.3}$$

The standard deviation of the distribution of samples (Δc^X) then follows naturally as:

$$\Delta c^X = \sqrt{\frac{\bar{C}^X (1 - \bar{C}^X)}{n_c}} \tag{A.4}$$

Using the relation of Eq. (A.4), random sampling of a multicomponent solute ensemble creates a set of Gaussian distributions of compositions: $G^X \sim \left(\bar{C}^X, \sqrt{\frac{\bar{C}^X(1-\bar{C}^X)}{n_c}}\right)$. Similar arguments for n_s random samples from a binary occupancy vector (S_i^{XY}) of pairings between solutes X and Y leads to a Gaussian distribution that can be parameterized as $G^{XY} \sim \left(\bar{C}^X\bar{C}^Y, \sqrt{\frac{\bar{C}^X\bar{C}^Y(1-\bar{C}^X\bar{C}^Y)}{n_s}}\right)$.

APPENDIX B: STANDARD DEVIATION OF THE PER ATOM PAIR INTERACTION ENERGY

The calculation of the standard deviation of the pair interaction energy term (ΔV) begins with a consideration of the types of pairwise interactions that are available to specific solutes in randomly arranged solid solutions. For instance, a solute of type X may interact with other solutes of type X or Y, forming pair interactions XX or XY. However, through the specification of atom type X as the solute of consideration, interactions of YX or YY are not considered and belong to a separate set of solute pairings (i.e., as in conditional probabilities). This nuanced point is significant, as it highlights a pathway to treat the statistical scatter that arises in pair interactions. That is, the statistical scatter of interactions can be viewed as an aggregation of separate solute pairing distributions that can be individually specified. Phrased differently, calculation of ΔV can be achieved through a separate determination of ΔV^X , where ΔV^X is the standard deviation of interaction energies between a central solute X and all other solute neighbors within the coordination cutoff. One additional complication is that the pair interaction energy is formed from the contributions of solute pairings from all neighbors. The distribution of interaction energies is therefore comprised of additive combinations, which can be treated using the central limit theorem of sums. Under these considerations, the solute-level standard deviations can be calculated through a weighted combination of variances in each of the coordination shells as:

$$\Delta V^X = \sqrt{\sum_{\zeta,Y} \left(V_{\zeta}^{XY} - \bar{V}_{\zeta}^X\right)^2 \bar{C}^Y N_{\zeta}}$$
(B.1)

where $\bar{V}_{\zeta}^{X} = \sum_{Y} V_{\zeta}^{XY} \bar{C}^{Y}$ is the average interaction energy for a solute X in coordination shell

 ζ . In addition to the solute-level standard deviation, the solute-level average of the interaction energy (\bar{V}^X) is also of interest. This term can be calculated from \bar{V}_{ζ}^X as:

$$\bar{V}^X = \sum_{\zeta} \bar{V}_{\zeta}^X N_{\zeta} = \sum_{\zeta, Y} V_{\zeta}^{XY} \bar{C}^Y N_{\zeta}$$
 (B.2)

In the formulation of Eq. (B.1), it is assumed that the variances between coordination shells are uncorrelated (i.e., their covariance is zero), which is appropriate for randomly arranged solid solutions. In both equations, the transformation of the statistical parameters of individual solute pair energies to the distribution of additive combinations of per atom pair interaction energies is achieved through the coordination number term, N_{ζ} , as per the central limit theorem of sums. Eq. (B.1) provides the standard deviations of the distribution pair interaction energies for each solute, which can be considered as non-overlapping sub-populations of a larger distribution. Under this consideration, the aggregated standard deviation (ΔV) of the system-level pair interaction energy term can then be calculated as a combination of the solute-level standard deviations as:

$$\Delta V = \sqrt{\sum_{X} \left[\Delta V^{X^2} + (\bar{V}^X - \bar{V})^2 \right] \bar{C}^X}$$
(B.3)

where \bar{V} is the system-level average pair interaction energy over all coordination shells. Eq. (B.3) can be viewed as a weighted linear combination of individual solute-level variances. The second term (difference of averages, $\bar{V}^X - \bar{V}$) is a correction term to account for differences between the sub-population and aggregate averages. Eq. (B.3) can be simplified further, without any loss of numerical accuracy, to eliminate the need to calculate \bar{V} . This simplified

relation appears as Eq. (6) in Section 2.1.

APPENDIX C: COVARIANCES OF STATISTICAL VARIABLES

This appendix provides derivations for two covariance terms used in the paper body: $cov\left(F,\frac{1}{2}V\right)$ and $cov(E^n,E^{FCC})$. In both derivations, the covariance is derived from its definition as the difference between the expectation value of products and the product of expectation values of the statistical variables. Beginning with the embedding and interaction energy distributions (i.e., $cov\left(F,\frac{1}{2}V\right)$), the covariance can be calculated from its expectation value definition as:

$$cov\left(F, \frac{1}{2}V\right) = \langle \frac{FV}{2} \rangle - \langle F \rangle \langle \frac{V}{2} \rangle \tag{C.1}$$

where the $\langle \rangle$ operator denotes the expectation value. Here, the individual expectation values of the embedding (i.e., $\langle F \rangle$) and pair interaction energies (i.e., $\langle V/_2 \rangle$) are given directly by the terms of Eq. (3). The expectation value of products (i.e., $\langle FV/_2 \rangle$) can be calculated from the sum of the products of $(F, V/_2)$ pairings weighted by their probability. In these pairings, F can be separated into solute-specific constants, whose probabilities are weighted by composition (i.e., $\bar{C}^X F^X$), as follows from the average per atom charge density assumption. Similarly, the pair interaction energy can also be decomposed into the separate distributions of solute-level interaction energies (i.e., V^X). These solute-level distributions are paired with $\bar{C}^X F^X$ coefficients, such that $\langle FV/_2 \rangle = \frac{1}{2} \sum_{X,i} \bar{C}^X F^X p_i V_i^X$, where p_i is the probability of obtaining V_i^X . The probability-weighted sum of V^X can be calculated from its expectation value, $\langle V^X \rangle = \sum_i p_i V_i^X = \bar{V}^X$, which is given by Eq. (B.2). Under these considerations, the

summation of the products of these terms (i.e., $\frac{1}{2}\sum_{X} \bar{C}^{X} F^{X} \bar{V}^{X}$) returns the expectation value of products. The covariance (Eq. (10) in the main text) can therefore be calculated as:

$$cov\left(F, \frac{1}{2}V\right) = \left\langle \frac{FV}{2} \right\rangle - \left\langle F \right\rangle \left\langle \frac{V}{2} \right\rangle$$
 (C.2a)

$$= \frac{1}{2} \sum_{X} \bar{C}^{X} F^{X} \bar{V}^{X} - \left(\sum_{X} \bar{C}^{X} F^{X} \right) \left(\frac{1}{2} \sum_{X,Y,\zeta} V_{\zeta}^{XY} N_{\zeta} \bar{C}^{X} \bar{C}^{Y} \right)$$
(C.2b)

Analysis of the covariance between the distributions of faulted and FCC-coordinated per atom energies begins with its definition as the differences of expectation values:

$$cov(E_a^n, E_a^{FCC}) = \langle E_a^n E_a^{FCC} \rangle - \langle E_a^n \rangle \langle E_a^{FCC} \rangle$$
 (C.3)

Individual expectation values (i.e., $\langle E_a^{FCC} \rangle$ and $\langle E_a^n \rangle$) are given directly by Eq. (3). However, in the latter calculation, the average energies in each of the m {111} layers influenced by the defect must first be calculated (i.e., $\bar{E}_a^{n,m}$). The average over all non-FCC layers (i.e., \bar{E}_a^n) is then calculated by the weighted sum of per atom average energies (i.e., $\frac{1}{M} \sum_m \bar{E}_a^{n,m}$).

The expectation value of products (i.e., $\langle E_a^n E_a^{FCC} \rangle$) can be separated into a summation of expectation values of the embedding (i.e., F^n , F^{FCC}) and pair interaction energy terms (i.e., V^n , V^{FCC}) in the faulted and fault-free conditions:

$$\langle E_a^n E_a^{FCC} \rangle = \langle \left(F^n + \frac{1}{2} V^n \right) \left(F^{FCC} + \frac{1}{2} V^{FCC} \right) \rangle$$

$$= \langle F^n F^{FCC} \rangle + \langle F^{FCC} \frac{1}{2} V^n \rangle + \langle F^n \frac{1}{2} V^{FCC} \rangle + \langle \frac{1}{2} V^n \frac{1}{2} V^{FCC} \rangle$$
 (C.4b)

Each of these expectation values of products can be further analyzed using arguments similar to those presented for the determination of $cov\left(F,\frac{1}{2}V\right)$ in Eq. (C.2b). For instance, the

expectation value of the product of embedding energy distributions (i.e., $\langle F^nF^{FCC}\rangle$) follows directly from the separation of these terms into their solute-level and fault plane-level constants (i.e., $F^{X,n,m}$ and $F^{X,FCC}$), whose probability of pairing is $\overline{C}^X/_M$. Here, M is the total number of non-FCC coordinated {111} planes within the cutoff radius of the planar defect. The expectation value then becomes the summation of paired embedding energies over all solute and faulted layers, $\langle F^n F^{FCC} \rangle = \frac{1}{M} \sum_{X,m} \bar{C}^X F^{X,n,m} F^{X,FCC}$. The expectation values of crossproducts (i.e., $\langle F^{FCC}V^n/2 \rangle$ and $\langle F^nV^{FCC}/2 \rangle$ follow from the expressions in Eq. (C.2b), with the embedding and pair interaction coefficients updated to reflect the summation over the fault $\langle F^{FCC}V^n/2 \rangle = \frac{1}{M} \sum_{X,m} \frac{1}{2} \bar{C}^X F^{X,FCC} \bar{V}^{X,n,m}$ and $\langle F^n V^{FCC}/2 \rangle =$ $\frac{1}{M}\sum_{X,m}\frac{1}{2}\bar{C}^XF^{X,n,m}\bar{V}^{X,FCC}$. Here, the embedding energies and averages of pair interaction energies (i.e., $\bar{V}^{X,FCC}$ and $\bar{V}^{X,n,m}$) are given by application of the appropriate coordination environments to Eq. (B.2). For the final expectation of products term, $\langle V^n/2, V^{FCC}/2 \rangle$, we assume that these distributions are independent of one another (i.e., $cov(V^n/2, V^{FCC}/2) =$ 0). This assumption enables a separation of the distribution products and a direct estimate for this term as $\langle V^n/2 V^{FCC}/2 \rangle \approx \langle V^n/2 \rangle \langle V^{FCC}/2 \rangle = \frac{1}{M} \sum_{X,m} \frac{1}{4} \bar{V}^{X,n,m} \bar{V}^{X,FCC}$. Although the distributions of V^n and V^{FCC} are likely correlated due to sharing some common neighbor pairings, we find that this approximation provides excellent estimates of covariances (see Figure C.1). Combining each of these expectation values delivers an approximate solution for the expectation value of products of distributions of per atom energies. Without further approximation, this equation can be factored and simplified in terms of the solute-level average per atom energies of the faulted and FCC distributions (i.e., $\bar{E}_a^{X,n,m}$ and $\bar{E}_a^{X,FCC}$) as:

$$\langle E_a^n E_a^{FCC} \rangle \approx \frac{1}{M} \sum_{X,m} \bar{C}^X \left(F^{X,n,m} F^{X,FCC} + \frac{1}{2} F^{X,FCC} \bar{V}^{X,n,m} + \frac{1}{2} F^{X,n,m} \bar{V}^{X,FCC} + \frac{1}{4} \bar{V}^{X,n,m} \bar{V}^{X,FCC} \right)$$

$$(C.5a)$$

$$\approx \frac{1}{M} \sum_{X,m} \bar{C}^{X} \bar{E}_{a}^{X,n,m} \bar{E}_{a}^{X,FCC}$$
 (C.5b)

The solute-level average per atom energies are defined here as:

$$\bar{E}_a^{X,n,m} = F^{X,n,m} + \frac{1}{2}\bar{V}^{X,n,m} \tag{C.6}$$

$$\bar{E}_a^{X,FCC} = F^{X,FCC} + \frac{1}{2}\bar{V}^{X,FCC} \tag{C.7}$$

where the \overline{V}^X is given by Eq. (B.2) in the corresponding coordination environment (i.e., faulted plane n, m or FCC). Insertion of Eq. (C.5b) into Eq. (C.3) delivers the final analytical expression for the covariance of per atom energies between the faulted and FCC distributions:

$$cov(E_a^n, E_a^{FCC}) = \langle E_a^n E_a^{FCC} \rangle - \langle E_a^n \rangle \langle E_a^{FCC} \rangle$$
 (C.8a)

$$\approx \frac{1}{M} \left(\sum_{X,m} \bar{C}^X \bar{E}_a^{X,n,m} \bar{E}_a^{X,FCC} - \bar{E}_a^{FCC} \sum_m \bar{E}_a^{n,m} \right)$$
 (C.8b)

This final relation appears as Eq. (14) in the main text. A numerical simulation was performed to assess the accuracy of the approximation made in the calculation of $\langle V^n/2 V^{FCC}/2 \rangle$. For this purpose, faulted topologies were computationally generated for a variety of randomly arranged solid solution single crystals with different compositions. The topologies of these crystals matched the idealized (i.e., unrelaxed) coordination environments of the faulted FCC systems considered in the GPFE landscape. The distribution of per atom energies is then calculated

through an atom-by-atom examination of chemistry and pair interactions, and the application of the relevant equations of the EAM potential. The expectation values and covariance terms of Eq. (C.3) are determined directly from these computational measurements. This process is similar to the initialization phase of MS calculations, where idealized crystal topologies are input into the MS software and the initial energies of atoms are computed. Numerical estimates of the covariances relevant to this study are provided in Figure C.1. These numerical results are overlaid with analytical estimates from Eq. (C.8b), showing excellent agreement. In addition, covariance values from MS relaxation calculations are also provided. These relaxed values also show excellent agreement with analytical estimates. The largest deviations are found in the equimolar NiCr sample, with all analytical covariance estimates showing less than $a\approx 4\%$ difference with the relaxed data.

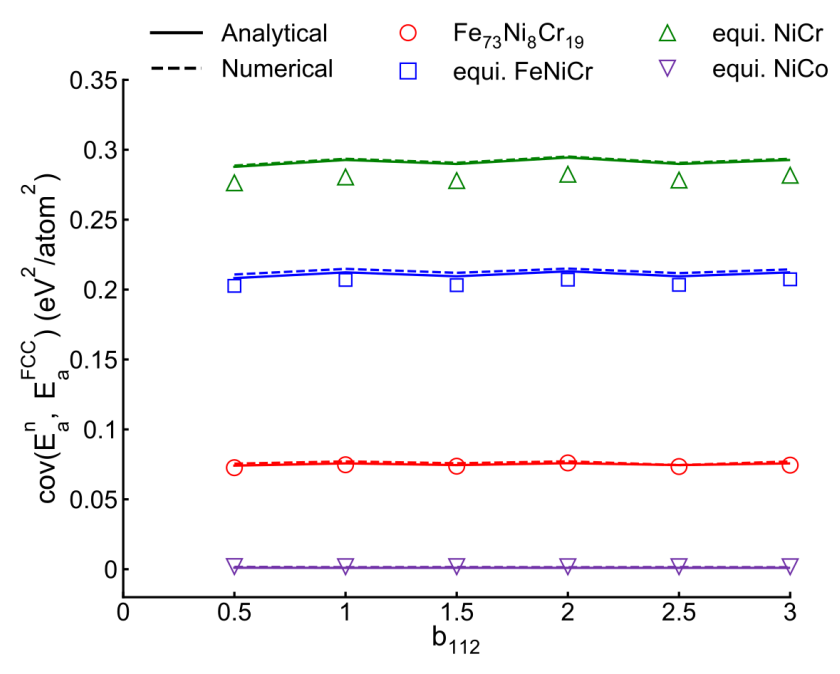


Figure C.1: The covariance between the distributions of FCC and faulted per atom energies across different planar faults. The distribution of faulted per atom energies includes contributions from all non-FCC coordinated {111} layers within the cutoff of the planar fault. Covariance predictions from analytical (Eq. (C.8b)) and numerical estimates are provided in solid and dashed stroke, respectively. Relaxed measurements from MS shearing calculations are shown as markers.

ACKNOWLEDGEMENTS

This material is based upon work supported by the National Science Foundation under Grant No. DMR-2144451. The authors gratefully acknowledge the Advanced Cyberinfrastructure for Education and Research (ACER) group at the University of Illinois at Chicago for providing computational resources and services needed to deliver research results delivered within this paper. URL: https://acer.uic.edu. The authors would also like to thank Ariana Sofia Del Valle for her assistance in maintaining and updating python scripts.

ADDITIONAL INFORMATION

Supplementary information is available in the online version of the paper.

DATA AVAILABILITY

Codes to reproduce these findings are available to download from https://github.com/dalymatt/Solid-Solution-PE-Statistics.

REFERENCES

- [1] D. Farkas, A. Caro, Model interatomic potentials and lattice strain in a high-entropy alloy, J. Mater. Res. 33 (2018) 3218–3225. doi:10.1557/jmr.2018.245.
- [2] W.-R. Jian, Z. Xie, S. Xu, Y. Su, X. Yao, I.J. Beyerlein, Effects of lattice distortion and chemical short-range order on the mechanisms of deformation in medium entropy alloy CoCrNi, Acta Mater. 199 (2020) 352–369. doi:10.1016/j.actamat.2020.08.044.
- [3] M.L. Ali, S. Shinzato, V. Wang, Z. Shen, J. Du, S. Ogata, An Atomistic Modeling Study of the Relationship between Critical Resolved Shear Stress and Atomic Structure Distortion in FCC High Entropy Alloys Relationship in Random Solid Solution and Chemical-Short-Range-Order Alloys —, Mater. Trans. 61 (2020) 605–609.

- doi:10.2320/matertrans.MT-MK2019007.
- [4] P. Wang, Y. Wu, J. Liu, H. Wang, Impacts of atomic scale lattice distortion on dislocation activity in high-entropy alloys, Extrem. Mech. Lett. 17 (2017) 38–42. doi:10.1016/j.eml.2017.09.015.
- [5] C.-C. Yen, G.-R. Huang, Y.-C. Tan, H.-W. Yeh, D.-J. Luo, K.-T. Hsieh, E.-W. Huang, J.-W. Yeh, S.-J. Lin, C.-C. Wang, C.-L. Kuo, S.-Y. Chang, Y.-C. Lo, Lattice distortion effect on elastic anisotropy of high entropy alloys, J. Alloys Compd. 818 (2020) 152876. doi:10.1016/j.jallcom.2019.152876.
- [6] S. Nag, W.A. Curtin, Effect of solute-solute interactions on strengthening of random alloys from dilute to high entropy alloys, Acta Mater. 200 (2020) 659–673. doi:10.1016/j.actamat.2020.08.011.
- [7] S. Nag, C. Varvenne, W.A. Curtin, Solute-strengthening in elastically anisotropic fcc alloys, Model. Simul. Mater. Sci. Eng. 28 (2020) 025007. doi:10.1088/1361-651X/ab60e0.
- [8] C. Varvenne, A. Luque, W.A. Curtin, Theory of strengthening in fcc high entropy alloys, Acta Mater. 118 (2016) 164–176. doi:10.1016/j.actamat.2016.07.040.
- [9] L. Zhang, Y. Xiang, J. Han, D.J. Srolovitz, The effect of randomness on the strength of high-entropy alloys, Acta Mater. 166 (2019) 424–434. doi:10.1016/j.actamat.2018.12.032.
- [10] E. Antillon, C. Woodward, S.I. Rao, B. Akdim, T.A. Parthasarathy, A molecular dynamics technique for determining energy landscapes as a dislocation percolates

- through a field of solutes, Acta Mater. 166 (2019) 658–676. doi:10.1016/j.actamat.2018.12.037.
- [11] C.R. LaRosa, M. Shih, C. Varvenne, M. Ghazisaeidi, Solid solution strengthening theories of high-entropy alloys, Mater. Charact. 151 (2019) 310–317. doi:10.1016/j.matchar.2019.02.034.
- [12] M. Sudmanns, J.A. El-Awady, The effect of local chemical ordering on dislocation activity in multi-principle element alloys: A three-dimensional discrete dislocation dynamics study, Acta Mater. 220 (2021) 117307. doi:10.1016/j.actamat.2021.117307.
- [13] C. Varvenne, G.P.M. Leyson, M. Ghazisaeidi, W.A. Curtin, Solute strengthening in random alloys, Acta Mater. 124 (2017) 660–683. doi:10.1016/j.actamat.2016.09.046.
- [14] M. Beyramali Kivy, M. Asle Zaeem, Generalized stacking fault energies, ductilities, and twinnabilities of CoCrFeNi-based face-centered cubic high entropy alloys, Scr. Mater. 139 (2017) 83–86. doi:10.1016/j.scriptamat.2017.06.014.
- [15] H. Huang, X. Li, Z. Dong, W. Li, S. Huang, D. Meng, X. Lai, T. Liu, S. Zhu, L. Vitos, Critical stress for twinning nucleation in CrCoNi-based medium and high entropy alloys, Acta Mater. 149 (2018) 388–396. doi:10.1016/j.actamat.2018.02.037.
- [16] S. Xu, E. Hwang, W.-R. Jian, Y. Su, I.J. Beyerlein, Atomistic calculations of the generalized stacking fault energies in two refractory multi-principal element alloys, Intermetallics. 124 (2020) 106844. doi:10.1016/j.intermet.2020.106844.
- [17] S. Zhao, Y. Osetsky, G.M. Stocks, Y. Zhang, Local-environment dependence of stacking fault energies in concentrated solid-solution alloys, Npj Comput. Mater. 5 (2019) 13.

- doi:10.1038/s41524-019-0150-y.
- [18] Y.H. Zhang, Y. Zhuang, A. Hu, J.J. Kai, C.T. Liu, The origin of negative stacking fault energies and nano-twin formation in face-centered cubic high entropy alloys, Scr. Mater. 130 (2017) 96–99. doi:10.1016/j.scriptamat.2016.11.014.
- [19] B. Xiao, L. Xu, C. Cayron, J. Xue, G. Sha, R. Logé, Solute-dislocation interactions and creep-enhanced Cu precipitation in a novel ferritic-martensitic steel, Acta Mater. 195 (2020) 199–208. doi:10.1016/j.actamat.2020.05.054.
- [20] A.S. Tirunilai, T. Hanemann, K.P. Weiss, J. Freudenberger, M. Heilmaier, A. Kauffmann, Dislocation-based serrated plastic flow of high entropy alloys at cryogenic temperatures, Acta Mater. 200 (2020) 980–991. doi:10.1016/j.actamat.2020.09.052.
- [21] G. Bracq, M. Laurent-Brocq, C. Varvenne, L. Perrière, W.A. Curtin, J.-M. Joubert, I. Guillot, Combining experiments and modeling to explore the solid solution strengthening of high and medium entropy alloys, Acta Mater. 177 (2019) 266–279. doi:10.1016/j.actamat.2019.06.050.
- [22] R. Labusch, A Statistical Theory of Solid Solution Hardening, Phys. Status Solidi. 41 (1970) 659–669. doi:10.1002/pssb.19700410221.
- [23] G.P.M. Leyson, W.A. Curtin, L.G. Hector, C.F. Woodward, Quantitative prediction of solute strengthening in aluminium alloys, Nat. Mater. 9 (2010) 750–755. doi:10.1038/nmat2813.
- [24] J.A. Yasi, L.G. Hector, D.R. Trinkle, First-principles data for solid-solution strengthening of magnesium: From geometry and chemistry to properties, Acta Mater.

- 58 (2010) 5704–5713. doi:10.1016/j.actamat.2010.06.045.
- [25] D. Ma, M. Friák, J. von Pezold, D. Raabe, J. Neugebauer, Computationally efficient and quantitatively accurate multiscale simulation of solid-solution strengthening by ab initio calculation, Acta Mater. 85 (2015) 53–66. doi:10.1016/j.actamat.2014.10.044.
- [26] W.G. Nöhring, W.A. Curtin, Design using randomness: a new dimension for metallurgy, Scr. Mater. 187 (2020) 210–215. doi:10.1016/j.scriptamat.2020.06.012.
- [27] E.P. George, W.A. Curtin, C.C. Tasan, High entropy alloys: A focused review of mechanical properties and deformation mechanisms, Acta Mater. 188 (2020) 435–474. doi:10.1016/j.actamat.2019.12.015.
- [28] C. Varvenne, A. Luque, W.G. Nöhring, W.A. Curtin, Average-atom interatomic potential for random alloys, Phys. Rev. B. 93 (2016) 104201. doi:10.1103/PhysRevB.93.104201.
- [29] M.S. Daw, M.I. Baskes, Embedded-atom method: Derivation and application to impurities, surfaces, and other defects in metals, Phys. Rev. B. 29 (1984) 6443–6453. doi:10.1103/PhysRevB.29.6443.
- [30] S.M. Foiles, M.I. Baskes, M.S. Daw, Embedded-atom-method functions for the fcc metals Cu, Ag, Au, Ni, Pd, Pt, and their alloys, Phys. Rev. B. 33 (1986) 7983–7991. doi:10.1103/PhysRevB.33.7983.
- [31] M.S. Daw, S.M. Foiles, M.I. Baskes, The embedded-atom method: a review of theory and applications, Mater. Sci. Reports. 9 (1993) 251–310. doi:10.1016/0920-2307(93)90001-U.
- [32] W.G. Nöhring, W.A. Curtin, Thermodynamic properties of average-atom interatomic

- potentials for alloys, Model. Simul. Mater. Sci. Eng. 24 (2016) 045017. doi:10.1088/0965-0393/24/4/045017.
- [33] S. Nag, T. Junge, W.A. Curtin, Atomistic-continuum coupling of random alloys, Model. Simul. Mater. Sci. Eng. 27 (2019) 075004. doi:10.1088/1361-651X/ab2c5c.
- [34] S.I. Rao, C. Woodward, T.A. Parthasarathy, O. Senkov, Atomistic simulations of dislocation behavior in a model FCC multicomponent concentrated solid solution alloy, Acta Mater. 134 (2017) 188–194. doi:10.1016/j.actamat.2017.05.071.
- [35] S.I. Rao, C. Varvenne, C. Woodward, T.A. Parthasarathy, D. Miracle, O.N. Senkov, W.A. Curtin, Atomistic simulations of dislocations in a model BCC multicomponent concentrated solid solution alloy, Acta Mater. 125 (2017) 311–320. doi:10.1016/j.actamat.2016.12.011.
- [36] T.M. Smith, M.S. Hooshmand, B.D. Esser, F. Otto, D.W. McComb, E.P. George, M. Ghazisaeidi, M.J. Mills, Atomic-scale characterization and modeling of 60° dislocations in a high-entropy alloy, Acta Mater. 110 (2016) 352–363. doi:10.1016/j.actamat.2016.03.045.
- [37] M. Shih, J. Miao, M. Mills, M. Ghazisaeidi, Stacking fault energy in concentrated alloys, Nat. Commun. 12 (2021) 3590. doi:10.1038/s41467-021-23860-z.
- [38] Q.-J. Li, H. Sheng, E. Ma, Strengthening in multi-principal element alloys with local-chemical-order roughened dislocation pathways, Nat. Commun. 10 (2019) 3563. doi:10.1038/s41467-019-11464-7.
- [39] E. Ma, Unusual dislocation behavior in high-entropy alloys, Scr. Mater. 181 (2020) 127–

- 133. doi:10.1016/j.scriptamat.2020.02.021.
- [40] G. Bonny, D. Terentyev, R.C. Pasianot, S. Poncé, A. Bakaev, Interatomic potential to study plasticity in stainless steels: the FeNiCr model alloy, Model. Simul. Mater. Sci. Eng. 19 (2011) 085008. doi:10.1088/0965-0393/19/8/085008.
- [41] V. Vítek, Intrinsic stacking faults in body-centred cubic crystals, Philos. Mag. 18 (1968) 773–786. doi:10.1080/14786436808227500.
- [42] V. Vítek, Multilayer stacking faults and twins on {211} planes in B.C.C. metals, Scr. Metall. 4 (1970) 725–732. doi:10.1016/0036-9748(70)90214-0.
- [43] E.B. Tadmor, S. Hai, A Peierls criterion for the onset of deformation twinning at a crack tip, J. Mech. Phys. Solids. 51 (2003) 765–793. doi:10.1016/S0022-5096(03)00005-X.
- [44] E.B. Tadmor, N. Bernstein, A first-principles measure for the twinnability of FCC metals, J. Mech. Phys. Solids. 52 (2004) 2507–2519. doi:10.1016/j.jmps.2004.05.002.
- [45] R.J. Asaro, S. Suresh, Mechanistic models for the activation volume and rate sensitivity in metals with nanocrystalline grains and nano-scale twins, Acta Mater. 53 (2005) 3369–3382. doi:10.1016/j.actamat.2005.03.047.
- [46] Z.H. Jin, S.T. Dunham, H. Gleiter, H. Hahn, P. Gumbsch, A universal scaling of planar fault energy barriers in face-centered cubic metals, Scr. Mater. 64 (2011) 605–608. doi:10.1016/j.scriptamat.2010.11.033.
- [47] M. Daly, A. Kumar, C.V. Singh, G. Hibbard, On the competition between nucleation and thickening in deformation twinning of face-centered cubic metals, Int. J. Plast. 130 (2020) 102702. doi:10.1016/j.ijplas.2020.102702.

- [48] M. Jo, Y.M. Koo, B.-J. Lee, B. Johansson, L. Vitos, S.K. Kwon, Theory for plasticity of face-centered cubic metals, Proc. Natl. Acad. Sci. 111 (2014) 6560–6565. doi:10.1073/pnas.1400786111.
- [49] R. Jagatramka, M. Daly, The Competition Between Deformation Twinning and Dislocation Slip in Deformed Face-Centered Cubic Metals, JOM. (2022). doi:10.1007/s11837-022-05437-3.
- [50] R.E. Kubilay, W.A. Curtin, Theory of twin strengthening in fcc high entropy alloys, Acta Mater. 216 (2021) 117119. doi:10.1016/j.actamat.2021.117119.
- [51] J. Ding, Q. Yu, M. Asta, R.O. Ritchie, Tunable stacking fault energies by tailoring local chemical order in CrCoNi medium-entropy alloys, Proc. Natl. Acad. Sci. 115 (2018) 8919–8924. doi:10.1073/pnas.1808660115.
- [52] J. Miao, C.E. Slone, T.M. Smith, C. Niu, H. Bei, M. Ghazisaeidi, G.M. Pharr, M.J. Mills, The evolution of the deformation substructure in a Ni-Co-Cr equiatomic solid solution alloy, Acta Mater. 132 (2017) 35–48. doi:10.1016/j.actamat.2017.04.033.
- [53] Y. Mishin, Interatomic Potentials for Metals, in: Handb. Mater. Model., Springer Netherlands, Dordrecht, 2005: pp. 459–478. doi:10.1007/978-1-4020-3286-8_23.
- [54] Advanced Materials and Microstructures Lab at the University of Illinois Chicago, Solid Solution PE Statistics, (n.d.). https://github.com/dalymatt/Solid-Solution-PE-Statistics (accessed June 29, 2022).
- [55] S. Plimpton, Fast Parallel Algorithms for Short-Range Molecular Dynamics, J. Comput. Phys. 117 (1995) 1–19. doi:10.1006/jcph.1995.1039.

- [56] A. Stukowski, Visualization and analysis of atomistic simulation data with OVITO-the Open Visualization Tool, Model. Simul. Mater. Sci. Eng. 18 (2010) 015012. doi:10.1088/0965-0393/18/1/015012.
- [57] P. Chowdhury, H. Sehitoglu, W. Abuzaid, H.J. Maier, Mechanical response of low stacking fault energy Co–Ni alloys Continuum, mesoscopic and atomic level treatments, Int. J. Plast. 71 (2015) 32–61. doi:10.1016/j.ijplas.2015.04.003.
- [58] M. Daly, S. Haldar, V.K. Rajendran, J. McCrea, G.D. Hibbard, C.V. Singh, Size effects in strengthening of NiCo multilayers with modulated microstructures, Mater. Sci. Eng. A. 771 (2020) 138581. doi:10.1016/j.msea.2019.138581.
- [59] Y.F. Shen, X.X. Li, X. Sun, Y.D. Wang, L. Zuo, Twinning and martensite in a 304 austenitic stainless steel, Mater. Sci. Eng. A. 552 (2012) 514–522. doi:10.1016/j.msea.2012.05.080.
- [60] G.B. Olson, M. Cohen, Kinetics of strain-induced martensitic nucleation, Metall. Trans.A. 6 (1975) 791–795. doi:10.1007/BF02672301.
- [61] T. Angel, Formation of Martensite in Austenitic Stainless Steel, J. Iron Steel Inst. 177 (1954) 165–174.
- [62] J.A. Venables, The martensite transformation in stainless steel, Philos. Mag. A J. Theor.Exp. Appl. Phys. 7 (1962) 35–44. doi:10.1080/14786436208201856.
- [63] Z.H. Aitken, V. Sorkin, Y.W. Zhang, Atomistic modeling of nanoscale plasticity in highentropy alloys, J. Mater. Res. 34 (2019) 1509–1532. doi:10.1557/jmr.2019.50.
- [64] T. Chen, L. Tan, Z. Lu, H. Xu, The effect of grain orientation on nanoindentation

- behavior of model austenitic alloy Fe-20Cr-25Ni, Acta Mater. 138 (2017) 83–91. doi:10.1016/j.actamat.2017.07.028.
- [65] P. Nash, Phase Diagram of Binary Nickel Alloys, ASM Int. (1991).
- [66] L.K. Béland, C. Lu, Y.N. Osetskiy, G.D. Samolyuk, A. Caro, L. Wang, R.E. Stoller, Features of primary damage by high energy displacement cascades in concentrated Nibased alloys, J. Appl. Phys. 119 (2016) 085901. doi:10.1063/1.4942533.
- [67] Y. Zhang, Y.J. Zhou, J.P. Lin, G.L. Chen, P.K. Liaw, Solid-solution phase formation rules for multi-component alloys, Adv. Eng. Mater. 10 (2008) 534–538.
- [68] S. Fang, X. Xiao, L. Xia, W. Li, Y. Dong, Relationship between the widths of supercooled liquid regions and bond parameters of Mg-based bulk metallic glasses, J. Non. Cryst. Solids. 321 (2003) 120–125. doi:10.1016/S0022-3093(03)00155-8.
- [69] C. Niu, C.R. LaRosa, J. Miao, M.J. Mills, M. Ghazisaeidi, Magnetically-driven phase transformation strengthening in high entropy alloys, Nat. Commun. 9 (2018) 1–9. doi:10.1038/s41467-018-03846-0.
- [70] Z. Zhang, H. Sheng, Z. Wang, B. Gludovatz, Z. Zhang, E.P. George, Q. Yu, S.X. Mao, R.O. Ritchie, Dislocation mechanisms and 3D twin architectures generate exceptional strength-ductility-toughness combination in CrCoNi medium-entropy alloy, Nat. Commun. 8 (2017) 14390. doi:10.1038/ncomms14390.
- [71] S. Zhao, G.M. Stocks, Y. Zhang, Stacking fault energies of face-centered cubic concentrated solid solution alloys, Acta Mater. 134 (2017) 334–345. doi:10.1016/j.actamat.2017.05.001.

- [72] N.L. Okamoto, S. Fujimoto, Y. Kambara, M. Kawamura, Z.M.T. Chen, H. Matsunoshita, K. Tanaka, H. Inui, E.P. George, Size effect, critical resolved shear stress, stacking fault energy, and solid solution strengthening in the CrMnFeCoNi high-entropy alloy, Sci. Rep. 6 (2016) 35863. doi:10.1038/srep35863.
- [73] G. Laplanche, A. Kostka, C. Reinhart, J. Hunfeld, G. Eggeler, E.P. George, Reasons for the superior mechanical properties of medium-entropy CrCoNi compared to highentropy CrMnFeCoNi, Acta Mater. 128 (2017) 292–303. doi:10.1016/j.actamat.2017.02.036.
- [74] R. Zhang, S. Zhao, J. Ding, Y. Chong, T. Jia, C. Ophus, M. Asta, R.O. Ritchie, A.M. Minor, Short-range order and its impact on the CrCoNi medium-entropy alloy, Nature. 581 (2020) 283–287. doi:10.1038/s41586-020-2275-z.
- [75] G. Bonny, N. Castin, D. Terentyev, Interatomic potential for studying ageing under irradiation in stainless steels: the FeNiCr model alloy, Model. Simul. Mater. Sci. Eng. 21 (2013) 085004. doi:10.1088/0965-0393/21/8/085004.